

# Charge Exchange Ion Energy Analyzer for the PFRC-2 Plasma Device

Senior Thesis  
Department of Physics  
Princeton University  
Fall 2021 - Spring 2022

Matthew Noah Notis  
Advised by Professor Samuel A. Cohen

This paper represents my own work in accordance with University regulations.

/s/ Matthew Noah Notis

# Abstract

This thesis describes the setup, calibration, and operation of the charge exchange ion energy analyzer (SC-IEA) designed for the Princeton Field Reverse Configuration 2 (PFRC-2) plasma device at the Princeton Plasma Physics Laboratory. The introduction sets forth the basic notions of energy distribution and temperature necessary for understanding the design and functionality of the SC-IEA. Section 2 presents a detailed description of the diagnostic system, presenting the theoretical models for the operation of its different components, specifically the curved-plate analyzer and the stripping cell. Section 3 discusses the calibration process and results for testing out the diagnostic with a known ion source, along with a discussion of how the calibration results fit with the theoretical model in Section 2. Section 4 discusses the desired properties for the connection between the diagnostic and the PFRC-2 as well as the plans for its installation.

This work was made possible by funding from the Department of Energy for the Summer Undergraduate Laboratory Internship (SULI) program as well as by an ARPA-E grant. This work is supported by the US DOE Contract No. DE-AC02-09CH11466.

# Contents

<b>1</b>	<b>Introduction</b>	<b>3</b>
1.1	Energy Distribution . . . . .	4
1.2	Charge Exchange Diagnostic . . . . .	7
1.3	Operation of the PFRC-2 . . . . .	10
<b>2</b>	<b>Description of Diagnostic System</b>	<b>13</b>
2.1	Description of the SC-IEA Hardware . . . . .	13
2.2	Energy Analyzer: Physical Model for Operation . . . . .	14
2.3	Measurement of Analyzer Properties . . . . .	21
2.4	Stripping Cell . . . . .	22
<b>3</b>	<b>Calibration</b>	<b>26</b>
3.1	Procedure . . . . .	26
3.2	Results for the Voltage-Energy Relation . . . . .	30
3.3	Results for the Resolution . . . . .	33
3.3.1	Applying Resolution to Real Signals . . . . .	37
3.4	Magnitude of the Signal on the Channeltron . . . . .	40
<b>4</b>	<b>Installation on the PFRC-2</b>	<b>45</b>
4.1	Port and Tubing Design . . . . .	45
4.2	Maintaining Vacuum . . . . .	47
<b>5</b>	<b>Conclusion</b>	<b>50</b>
	<b>References/Acknowledgements</b>	<b>52</b>

# 1 Introduction

This thesis describes the setup, the calibration, and the installation of a charge-exchange ion energy diagnostic to measure the ion energy distribution on the Princeton Field Reversed Configuration 2 (PFRC-2) plasma device. This introductory section attempts to clarify all of the terms in the above sentence in a way that provides an understanding of the motivation and goal of the project, specifically focusing on describing the notion of an energy distribution, heating, and a charge-exchange diagnostic.

Firstly, it is important to clarify the basic notion of a plasma. The definition presented in *Principles of Plasma Physics* (Chen 1974), [1], is that a plasma is a “quasineutral gas of charged and neutral particles that exhibits collective behavior.” Quasineutrality indicates that on the whole, the gas is not charged, although individual pieces of the plasma may be charged. The positive particles, called ions, that make up plasma come from atoms that have been stripped from a certain number of their electrons and the negative particles come from the electrons that have been freed from being bound to individual atoms. Collective behavior is a way of distinguishing a plasma from a normal gas which also has a slight fraction of ionized particles. Because of the long range electromagnetic force, one part of the plasma influences other parts of the plasma. This property leads to effects such as waves and instabilities that contribute to the overall behavior of the plasma.

One of the most important concepts regarding the motion of charged particles in a magnetized plasma is that charged particles roughly follow magnetic field lines<sup>1</sup>. This can be seen from the equation of motion of a charged particle of mass  $m$  and charge  $q$  in a uniform magnetic field  $\vec{B} = B\hat{z}$ . The particle obeys the Lorentz force law with  $\vec{F} = q\vec{v} \times \vec{B}$ . This vector equation can be written as three separate equations:

$$\begin{aligned}m\frac{dv_x}{dt} &= qBv_y \\m\frac{dv_y}{dt} &= -qBv_x \\m\frac{dv_z}{dt} &= 0\end{aligned}$$

The solution to these equations, found by differentiating once more with respect to time and decoupling, is that the particle gyrates around the magnetic field line in the  $xy$

---

<sup>1</sup>This derivation follows that of Chen (1974), [1].

plane with a frequency of  $\omega_c = \frac{qB}{m}$ , called the cyclotron frequency, while traveling with constant velocity in the  $\hat{z}$  direction. Thus, the motion of a charged particle is helical, with the particle following the direction of a field line and staying within a set radius in any given  $xy$  plane. This single-particle motion is the reason that closed field lines are so significant to plasma confinement. There are many other effects that the single particle will feel in magnetic fields of varying strengths and directions, but much of that behavior can be described as velocity drifts in addition to the basic behavior of gyrating motion along a field line [1].

## 1.1 Energy Distribution

This section describes the notion of an energy distribution in a collection of particles. The energy of a gas can be described with a distribution function of the energies of the particles in the gas. The distribution function operates like a probability distribution, i.e. the fraction of particles in the gas with energy  $E \in [E_1, E_2]$  is given by  $\int_{E_1}^{E_2} f(E)dE$ . The Maxwell-Boltzmann, or Maxwellian, Distribution describes the energy distribution of a thermalized gas of classical particles [2]. To find the Maxwellian energy distribution for a collection of particles, one begins by finding the Maxwellian speed distribution<sup>2</sup>. The speed distribution function,  $f(v)$ , will be the product of the probability that the particle will have the velocity,  $v$ , multiplied by the number of possible velocity vectors corresponding to that speed. The probability term is given by Boltzmann statistics itself, in which the probability that a particle is in a particular state with energy  $E$  is proportional to  $e^{-E/kT}$ , where  $T$  is the temperature of the gas. Here, the state of velocity  $v$  corresponds to an energy given by  $E = \frac{1}{2}mv^2$ , so the probability that the particle has velocity  $v$  is proportional to  $e^{-mv^2/2kT}$ . The number of possible velocity vectors corresponding to a given speed  $v$  is given by thinking of the the velocities in a velocity space. In this case, each speed  $v$  corresponds to a spherical surface in this space with area  $4\pi v^2$ . Thus, the distribution function  $f(v)$  is proportional to  $4\pi v^2 e^{-mv^2/2kT}$ . By normalizing this so that  $f(v)dv$  integrates to 1, the distribution is found to be, [2]:

$$f(v) = \left(\frac{m}{2\pi kT}\right)^{3/2} 4\pi v^2 e^{-mv^2/2kT}. \quad (1)$$

To convert this into an energy distribution function, one uses the definition that  $E = \frac{1}{2}mv^2$  and  $dE = mv dv$ . Rearranging this, one finds that  $dv = \frac{dE}{\sqrt{2mE}}$ . Substituting these

---

<sup>2</sup>The following derivation comes from *Thermal Physics* (2000) by Daniel V. Schroeder, [2].

into the distribution function, one finds that:

$$f(v)dv = \sqrt{\frac{2}{\pi}} \frac{\sqrt{m}}{(kT)^{3/2}} mv^2 e^{-mv^2/2kT} dv = \sqrt{\frac{2}{\pi}} \frac{\sqrt{m}}{(kT)^{3/2}} 2E e^{-E/kT} \frac{1}{\sqrt{2mE}} dE. \quad (2)$$

Rearranging, the final energy distribution function becomes:

$$f(E) = \frac{2\sqrt{E}}{\sqrt{\pi}(kT)^{3/2}} e^{-E/kT}. \quad (3)$$

The Maxwell-Boltzmann distribution as a function of ion speed and ion energy are plotted below in Figures 1 and 2.

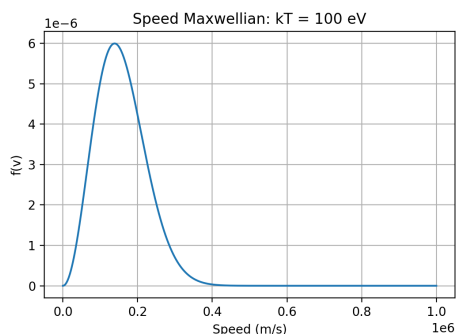


Figure 1: Maxwellian distribution plotted as a function of speed.

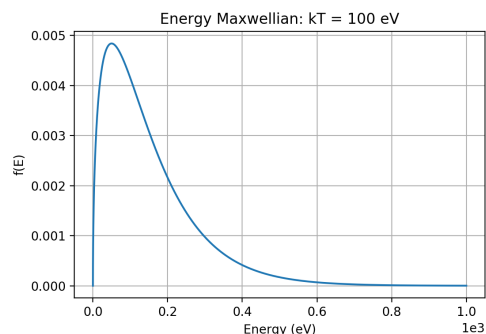


Figure 2: Maxwellian distribution plotted as a function of energy.

Even for classical gases, if the gas particles' velocities are not sufficiently randomized, the distribution function may not be a Maxwellian one. In other words, there must be a certain level of randomness to the velocities of the particles in question for their distribution to be characterized by a Maxwellian distribution. This randomization is termed the heating of particles and the achievement of heating in the PFRC-2 will be discussed further in Section 1.3 [3]. For now, it is enough to mention that the notion of a plasma's temperature depends on the plasma having a Maxwellian distribution, i.e. in the context of a gas, temperature  $T$  is only a meaningful concept with reference to a Maxwellian distribution.

The temperature of a plasma is often used to refer to  $kT$ , rather than  $T$ , and will have units of eV, where  $1 \text{ eV} = 1.602 * 10^{-19} \text{ J}$ . For a Maxwellian distribution, the

average energy  $\bar{E}$  can be found by taking the integral:

$$\bar{E} = \int_0^\infty E f(E) dE = \int_0^\infty \frac{2}{\sqrt{\pi}(kT)^{3/2}} E^{3/2} e^{-E/kT}. \quad (4)$$

Because of the  $E^{3/2}$  dependence, it is easier to evaluate this integral in velocity space. When this is done, as in [2], one finds that  $\bar{E} = \frac{1}{2}kT$ . Speaking about the temperature in terms of  $kT$  is thus a convenient way of noting the average energy of the distribution.

In a plasma, the different species, such as the different types of ions and the electrons, can have different energy distributions, which becomes an important fact when one wants to heat a plasma to high enough temperatures to allow for fusion to occur [1]. Although to a certain degree, because of attraction between like charges, the ions should generally follow the electrons, they can still have a distinct energy distribution. Knowledge of the ion energy distribution (IED) in particular is important in determining if a plasma is relevant for fusion. Fusion may occur when two nuclei approach each other with enough energy to overcome the Coulomb repulsion that normally attends the meeting of like charges. When the particles are energetic enough they approach close enough for the nuclear forces that make fusion energetically favorable to overcome the Coulomb repulsion barrier [1].

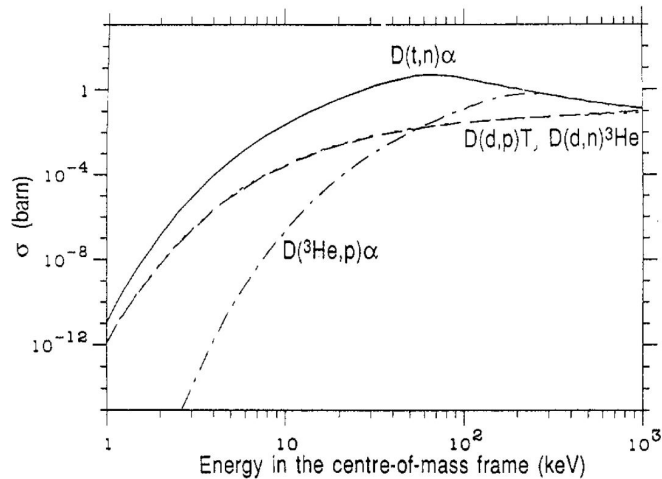


Figure 3: Collisional cross sections for three different fusion reactions, from Bosch and Hale (1992), [4].

The collisional cross sections for four different fusion reactions, D-<sup>3</sup>He, D-T, D-<sup>4</sup>He, and T-<sup>4</sup>He, as a function of energy are plotted in Figure 3. The cross sections are

expressed in units of barns, where 1 barn is equal to  $10^{-24}$  cm<sup>2</sup>, so one can see how unlikely the occurrence of the reaction is unless the ions have energies on the order of tens or hundreds of keV. The main result evident from this plot is that practical fusion depends on the existence of a population of ions with energies high enough for the fusion cross section to be non-negligible, i.e. the ion energy distribution needs to be sufficiently populous at high energies. To make this possible, there need to be methods of heating the ion species to high enough temperature, as well as diagnostics for assessing what the ion energy distribution is to see how ion heating occurs. The method for heating ions in the PFRC-2 will be discussed in Section 1.3, and the method for measuring the IED will be discussed in the next section, Section 1.2.

## 1.2 Charge Exchange Diagnostic

The charge exchange ion energy analyzer under present discussion is a diagnostic to measure the ion energy distribution in the plasma<sup>3</sup>. The main issue in analyzing ions in a plasma is that ions, as charged particles, should be confined with the magnetic fields. Even when they do escape, the particles do not carry information about the state of the plasma's interior because they experience forces as they exit the plasma that modify their energy and direction. One solution to this problem is to look at the flux of fast neutrals exiting the plasma, which is likely the product of charge exchange. The principle behind charge exchange is that when heated ions in the plasma's interior pass by unheated neutrals, there is some probability that the neutral will lose an electron to the ion, neutralizing the hot ion and allowing it to escape from the plasma. The reaction can be written as:



Because the two species have about the same mass, they retain their energies after the collision, and the new fast neutral can escape the confining fields and convey information about the ion energy distribution [5].

Hutchinson describes this as a quantum mechanical resonance phenomenon, i.e. when the two atoms with electrons come close to one another, the wavefunction describing an electron bound to the first atom can leak probability into another wavefunction describing the electron bound to the second atom. This process is maximized when the

---

<sup>3</sup>The principles of this diagnostic are described in Chapter 8 of *Principles of Plasma Diagnostics* by I. H. Hutchinson (1987).

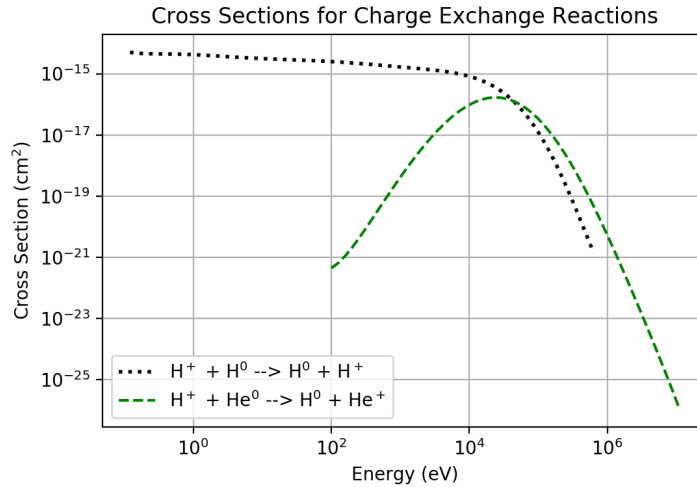


Figure 4: Cross sections for two charge exchange processes. Data is taken from C. F. Barnett (1990) and available on <https://www-amdis.iaea.org/ALADDIN/>.

two wavefunctions are very similar, which is why the data in Figure 4 shows very different behavior for the two reactions<sup>4</sup>. The  $H^+ + H^0$  reaction displays an almost constant cross section from  $\approx 1$  eV - 10 keV. On the other hand, the  $H^+ + He^0$  cross section has a very localized maximum value between 10 keV and 100 keV, steeply dropping off around that value. The difference is that the  $H^+ + H^0$  is a resonant one, so the probability of losing an electron is highest for low energies and stays fairly constant, whereas the  $H^+ + He^0$  reaction is non-resonant so it depends on there being a high incoming ion energy. This distinction is referred to in Rapp (1960), [6]. Because of the resonance, the charge exchange cross section along the whole range of interest for this experiment, about 100 eV - 1 keV, only changes by less than  $10^{-15}$  cm<sup>2</sup>, with a cross section of  $\approx 2.5 * 10^{-15}$  cm<sup>2</sup> for 100 eV and  $\approx 1.7 * 10^{-15}$  cm<sup>2</sup> for 1 keV. This is an important feature for the diagnostic, since it means that the energy distribution of ions will not be significantly shifted to higher or lower energies because of varying charge exchange cross section over the energy range.

The above process will produce a flux of neutral atoms exiting the machine that can then be analyzed to reveal information about the plasma's interior. Before the atoms

<sup>4</sup>A rough outline for the physical process appears in Exercise 8.1 and 8.2 in Hutchinson (1987). Time dependent perturbation theory can be used to calculate the probability that an electron with  $\psi_0^1$  will transfer to be bound to atom 2 in the ground state,  $\psi_0^2$ , given the perturbation potential of  $V(r) = \frac{e^2}{4\pi\epsilon_0 r}$ . The probability is given by  $P_{12} = |\langle \psi_0^2 | V | \psi_0^1 \rangle t / \hbar|^2$ .

can be analyzed, they need to be ionized. This has primarily been accomplished in the past in two different ways. One method uses a gas stripping cell with a region of high pressure gas so that the neutrals can collide and lose electrons to other neutral atoms as in Colchin (1988), [7]. The other method uses a solid foil that the atoms pass through, colliding with atoms to which they lose electrons as in Beiersdorfer (1987), [8]. The present system uses the former method.

The newly ionized flux is then analyzed using either electric or magnetic fields, or a combination of the two. The principle of these analyzers is to set up a field that splits the beam of incoming ions so that only ions with desired values of either energy or momentum will exit the analyzer and continue on to be tested. Analyzers that use electric fields select for ion energy, as in Eubank (1963), [9], and Beiersdorfer (1987) [8], while analyzers that use magnetic fields select for ion momentum. Combination of both magnetic and electrostatic analyzers allows one to separate the outgoing flux by particle mass as well, as in [10] and [11]. Because the flux in the present system is expected to be primarily of only one species,  $H^0$ , the use of a combined magnetic and electrostatic system would not be significantly more beneficial than a much simpler electrostatic-only analyzer. Thus, the analyzer in the present system is an electrostatic analyzer, the principles and operation of which will be discussed in further detail later.

For clarity and comparison, the basic principles of the magnetic analyzer will briefly be discussed. The principle is to set up a magnetic field such that an incoming beam in the plane perpendicular to the uniform magnetic field undergoes circular motion around the field. The radius executed by the ion is found by equating the Lorentz force law with the equation for centripetal force:

$$F = qvB = ma_c = m\frac{v^2}{r} \longrightarrow r = \frac{mv}{qB}. \quad (6)$$

Since  $p = mv$ , the magnetic field selects for  $r = \frac{p}{qB}$ , so the analyzer selects for momentum, which is directly proportional to the radius of the beam.

After the desired momentum or energy is selected from the beam, the selected ions from the beam can be measured and their signal recorded. In this system, the measurement of the ion flux is performed using an electron multiplier, which produces a pulse of  $\approx 10^7$  electrons for each ion that strikes the surface of the multiplier. These pulses are then detected in an oscilloscope.

### 1.3 Operation of the PFRC-2

This section introduces the basic concepts in the physics of field reversed configuration (FRC) devices in general and the Princeton FRC in particular, clarifies how heating of ions occurs, and how this affects the placement of and expected flux into the SC-IEA. The anatomy of a field reversed configuration is described in Steinhauer (2011), [12]. An FRC establishes a toroidal plasma without any central field coils, allowing for a device geometry that is much simpler than other toroidal devices. There are two main regimes of magnetic field geometries in an FRC. Inside of the separatrix, the magnetic field lines, pictured as the solid black lines in Figure 5, close in a toroidal shape, while outside the separatrix, the field lines open, leading to either end of the linear device [12]. The significance of open and closed field lines is such that particles in closed field lines are generally confined to the torus inside the machine, while particles on open field lines generally follow those field lines and escape from the machine. This is due to the basic helical motion of a charged particle along a field line described at the beginning of Section 1.

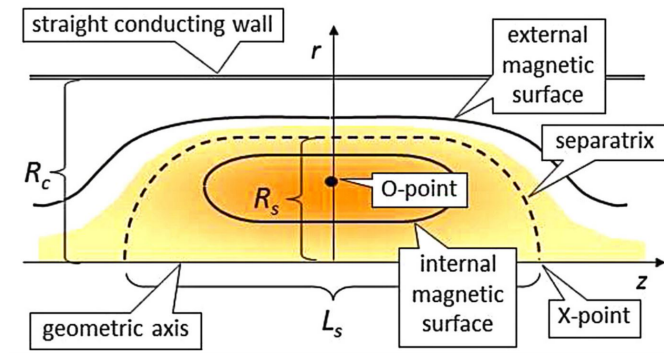


Figure 5: Schematic of FRC, taken from Steinhauer [12].

One of the ways of establishing and heating the particles in an FRC is through a rotating magnetic field (RMF), which is the addition of a transverse magnetic field with a direction that changes in time [12]. The term transverse in this context means that the magnetic field lines are in the plane perpendicular to the  $z$  axis [13]. The RMF rotates around the  $z$  axis, driving current as the ions and electrons follow the magnetic field lines. This current forms the toroidal field that confines the plasma in this configuration [12]. Past experiments of RMF driven FRCs resulted in poor energization and confinement. As suggested in [13], this was partly due to the fact that the type of RMF used in previous experiments broke down the closedness of the toroidal field lines. The Princeton FRC

(PFRC) configuration uses an RMF which has odd parity about the midplane ( $z = 0$  plane). The transverse component of this RMF is the solid black curve pictured in Figure 6, which has been shown to preserve the closed nature of magnetic field lines within the separatrix [13].

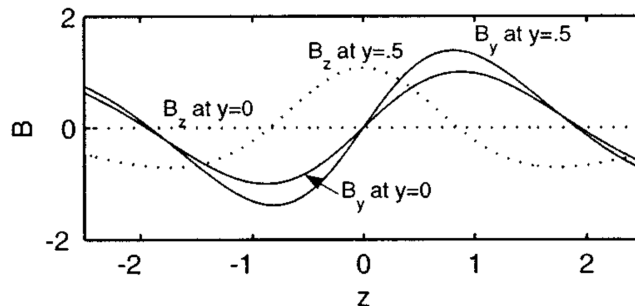


Figure 6: The transverse odd-parity magnetic field, from Cohen [13].

It has also been demonstrated using single particle codes that analyze the orbits of ions and electrons in the PFRC by integrating Hamilton's equations that the RMF<sub>o</sub> system not only establishes an FRC but also effectively heats electrons and ions [14]. The source of this heating is discussed both analytically and numerically by analyzing the energization of the three different types of particle orbits in the PFRC [3]. There are three different classes of orbits in the PFRC device, as discussed by Landsman in [15]. These orbits, which depend on the particle's momenta, termed cyclotron, betatron, or figure-8 orbits, are pictured in Figure 7. The figure-8 orbits are shown to exhibit the most heating from the RMF<sub>o</sub>. This is due to the fact that velocity randomization is necessary for heating, and the figure-8 orbits have more opportunities to fall out of phase with the RMF<sub>o</sub> and thus to experience velocity randomization. Further, because they are highly non-linear, slight variations in their initial conditions produce a chaotic selection of different states [3]. This method has also been experimentally verified to produce heating of particles in the PFRC [16].

To determine the proper placement of the charge exchange diagnostic, a simulation called the Synthetic Diagnostic (SD) code, created and implemented by Alan Glasser and by Samuel Cohen, was used to model the expected fluxes and energies of neutrals given different viewing chords of the diagnostic into the PFRC-2. Because of the different particle orbits, as shown in Figure 7, different viewing chords may see only certain populations of orbits. The final choice in the implementation of the system is that the

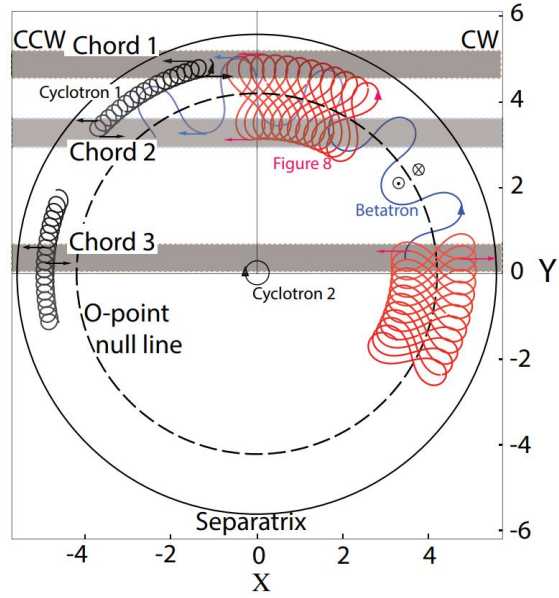


Figure 7: Possible orbits and their viewing chords in the PFRC-2, from an upcoming paper by Samuel A. Cohen in *Physics of Plasmas*.

diagnostic will be installed to view along the midline (major axis) of the system, but will have the ability to view at different angles within the plane of the major axis of the system, due to the likelihood that neutrals will exit with some nonzero velocity component in the  $\hat{z}$  direction. The plans for the connection and placement of the diagnostic onto the PFRC-2 will be discussed further in Section 4.

## 2 Description of Diagnostic System

This section describes the setup and physical principles essential to the operation of the charge exchange diagnostic. The section begins by discussing the hardware and overall structure of the diagnostic (2.1) before delving into the physics of the energy analyzer, clarifying the mechanics of its energy selection and other features (2.2) with some of the measurements of its features presented (2.3). Then, the principles behind the operation of the stripping cell are presented (2.4)

### 2.1 Description of the SC-IEA Hardware

As outlined above in Section 1.2, the diagnostic consists of three main stages: ionization, energy selection, and signal detection. Ionization is performed by placing a region of higher pressure in the path of the neutral flux. This region is called the stripping cell and is the thin metal tube pictured in between the two port crosses in Figure 8. Energy selection is performed in the curved-plate electrostatic ion energy analyzer, pictured below in Figure 9. This analyzer functions by establishing equal and opposite voltages on two concentric curved plates in such a way that ions of selected energy,  $E_0$ , are allowed to pass through the analyzer. Signal detection is accomplished using a Channeltron electron multiplier (Model 5901), in which each incoming ion that strikes the electron multiplier is converted into about  $10^7$  electrons that constitute the pulses that are observed by the oscilloscope.

The system setup, pictured in Figure 8, was designed and its parts were purchased by Eugene Evans in 2019. The basic setup is of two port crosses joined together in the center by the stripping cell. In the picture, the neutral flux enters from the right, passing through the stripping cell before exiting to the left to be analyzed in the curved-plate analyzer and detected in the electron multiplier.

There are several vacuums, gauges, and probes on the system to effectuate the above three main stages. A turbomolecular pump, directly underneath the port cross closest to the machine side, is able to keep the system pumped down to a pressure on the order of  $\approx 10^{-8}$  Torr, and there are two non-evaporative getter (NEG) pumps nestled in the interior of the two port crosses on either side of stripping cell. These pumps are important in the operation of the stripping cell, in which the stripping cell should have a gas pressure on the order of  $10^{-3}$  or  $10^{-2}$  Torr, while the rest of the system should still stay at a lower pressure to minimize scattering of the neutral flux in both energy and

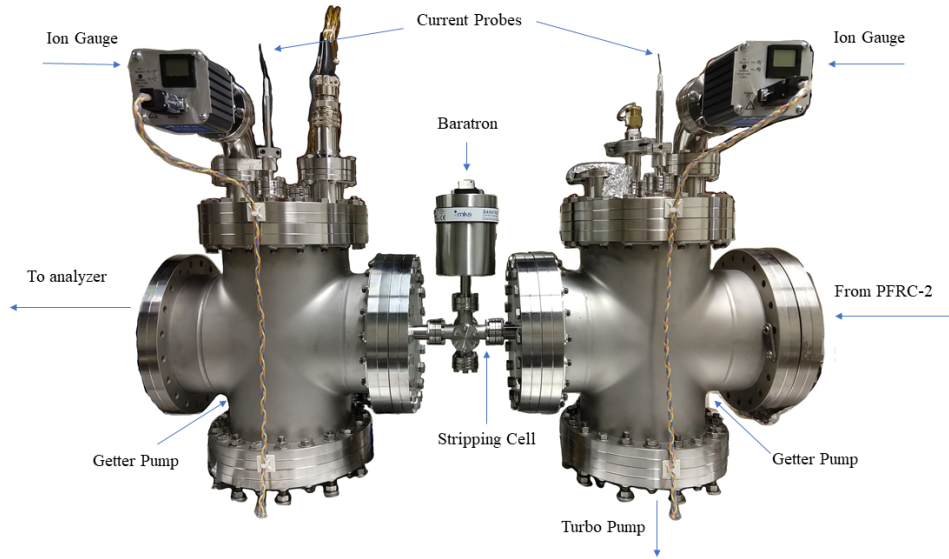


Figure 8: Photograph of the diagnostic setup with the main components labelled.

angle. At the top of each port cross is an ion gauge to measure pressure in the vessel. The ion gauges are sensitive up to  $\approx 10^{-10}$  Torr. There is a Baratron pressure gauge on the stripping cell, with a much lower sensitivity but one that suffices for the high pressure meant to be present in the stripping cell. Finally, there are two current probes created by Bruce Berlinger that hang down from the top of the port crosses that serve to measure the current of the ion beam during calibration but could also be helpful in the operation of the diagnostic on the plasma device. The system was constructed by Bruce Berlinger.

## 2.2 Energy Analyzer: Physical Model for Operation

The heart of the charge exchange diagnostic is the electrostatic curved plate analyzer. Consisting of two concentric curved metal plates subtending an angle of roughly  $90^\circ$  and separated by a distance,  $d$ , pictured in Figure 9, the analyzer operates by setting up a radial electric field in between the two plates that points towards the center of the analyzer's curvature. By varying the electric field, one can select a specific ion energy to execute a circular orbit, entering the aperture at one radius and exiting on the other end of the curved plates at the same radius such that it will be detected in the electron multiplier. This section will discuss the theory of operation behind the electrostatic

electron multiplier, seeking to clarify the way an electric field is established in between the plates and the derivation of both circular and nearly circular ion orbits in the electric field. These mechanics will then be applied to discuss the properties of such an analyzer, specifically its resolution. An analysis of these aspects of the energy analyzer will clarify how precisely and accurately these properties need to be determined for the successful operation of the system as an ion energy diagnostic on the PFRC-2.

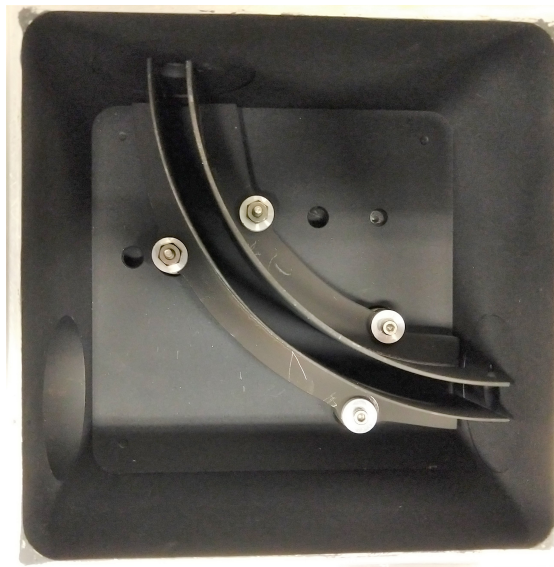


Figure 9: Picture of the curved-plate energy analyzer to be used in the SC-IEA.

Understanding the electric field in the energy analyzer is the foundation for all other investigations into its properties and uses. The electric field is established by setting up a voltage difference between the plates, with the inner plate set to  $V_-$  and the outer plate set to  $V_+$ . The geometry of the plates makes it difficult to solve analytically for the electric field for two reasons. First, the plates do not continue around the full circle but stop after  $90^\circ$ . Secondly, the extent of the plates in the direction orthogonal to the plane of the circle they surround (the  $\hat{z}$  direction) is not infinite. For these two reasons, the analyzer's geometry is one that is not simple to handle analytically. However, if one assumes that the electric field in the analyzer is approximately that of a cylindrically symmetric one with the asymmetries only greatly affecting the field near the edges of the analyzer, it is possible to analytically solve for the electric field and then discuss the effects of the asymmetries on the electric field and the paths of the ions. The discussion here will therefore focus on the properties in the case of cylindrical symmetry, with later discussion on how accurately this model applies to the present case.

To solve for the electric field in the case of cylindrical symmetry, one first solves for the electric potential using Poisson's equation and then applies the negative gradient to find the electric field. For a problem with cylindrical symmetry, this is:

$$\nabla^2\phi = 0 \longrightarrow \frac{1}{r} \frac{\partial}{\partial r} \left( r \frac{\partial}{\partial r} \right) \phi = \frac{\partial^2\phi}{\partial r^2} + \frac{1}{r} \frac{\partial\phi}{\partial r} = 0 \quad (7)$$

. This differential equation is an equidimensional equation. Testing out  $\phi = r^m$ , it is found that  $m = 0$  with multiplicity 2. Thus, the solution takes the form of  $\phi(r) = A + B \ln(r)$ . In order to find the solution for the energy analyzer, the boundary conditions of  $\phi(a) = V_-$  and  $\phi(b) = V_+$  need to be applied. After doing so, the potential is found to be

$$\phi(r) = V \left[ \frac{\ln(a) + \ln(b)}{\ln(a) - \ln(b)} - \frac{2 \ln(r)}{\ln(a) - \ln(b)} \right]. \quad (8)$$

Taking  $E = -\nabla\phi = -\frac{\partial\phi}{\partial r}$ , the electric field is found to be:

$$\vec{E}(r) = -\frac{2V}{\ln\left(\frac{b}{a}\right)} \frac{1}{r} \hat{r}. \quad (9)$$

The electric field in the cylindrically symmetric case is therefore found to be purely radial and varies with radius as  $\frac{1}{r}$ .

The voltage that enables a circular orbit for an ion of energy  $E_0$  is found by using the equation for circular motion:  $\vec{F} = -m\frac{v^2}{r}\hat{r}$ . In this case, the Coulomb force law states that  $\vec{F} = q\vec{E}$ , so one may write:

$$m\frac{v^2}{r} = q\frac{2V}{\ln\left(\frac{b}{a}\right)} \frac{1}{r}. \quad (10)$$

By using the definition of  $E_0 = \frac{1}{2}mv^2$ , one may reformulate Equation 10 as

$$V(E_0) = \frac{E_0 \ln\left(\frac{b}{a}\right)}{q}. \quad (11)$$

Thus, when the above voltage is applied, ions of energy  $E_0$  will execute circular motion and enter the aperture at the end of the curved plates. Equivalently, the proper voltage to apply to the plates to select for ions of energy  $E_0$ , when  $E_0$  is measured in electron volts (eV), is simply given by  $V(E_0) = \ln\left(\frac{b}{a}\right) * E_0$ . This equation is presented in Beiersdorfer (1987), [8], as well.

Inevitably, even if the plates in the analyzer are set to the proper voltages of  $\pm V(E_0)$ , some ions of energy  $E$  which is larger or smaller than  $E_0$  will be able to enter the aperture, strike the electron multiplier, and contribute to the signal. To calculate what range of  $E$  will still be detected, one needs to calculate the ion trajectory of a particle of energy  $E$  in an electric field set up to select for particles of energy  $E_0$ <sup>5</sup>. Because the electric field is assumed to be radial, the problem can be formulated as that of a particle in a central force field. To solve for the trajectory of such a particle,  $r(\theta)$ , it is convenient to begin with Binet's Equation<sup>6</sup>, a second-order differential equation for  $u(\theta)$ , where  $u = 1/r$ , in the case of a central force field:

$$\frac{d^2u}{d\theta^2} + u = -\frac{F(1/r)m}{l^2u^2}, \quad (12)$$

where  $l$  is the angular momentum of the particle. Plugging in  $F = q\frac{2V}{\ln(\frac{b}{a})}\frac{1}{r}$ , Equation 12 becomes

$$\frac{d^2u}{d\theta^2} + u = \frac{2mE_0}{l^2} \frac{1}{u}. \quad (13)$$

By rewriting the  $l^2$  in terms of  $E$ ,  $l^2$  becomes  $2mEr_0^2$ , where  $r_0$  is the radius of the entrance aperture. With this simplification,  $\frac{2mE_0}{l^2} = \frac{E_0}{Er_0^2}$ . To make the differential equation dimensionless, one lets  $y = u/u_0$ , where  $u_0$ , the characteristic inverse length, is defined as  $u_0 = \sqrt{\frac{E_0}{E}} \frac{1}{r_0}$ . With this, Equation 13 simplifies to the non-dimensional form of:

$$\frac{d^2y}{d\theta^2} + y = \frac{1}{y}. \quad (14)$$

Because of the equation's nonlinearity in  $y$ , it does not admit a closed-form analytic solution, so it is most easily solved through an approximation. Because the physical case of interest is when the trajectories are near circular, i.e. when  $u \approx u_0$ , letting  $y = 1 + x$ , where  $x$  is a small perturbation, will produce an approximate solution to the problem. Plugging in  $y = 1 + x$  and making use of the expansion  $\frac{1}{1+x} \approx 1 - x + O(x^2)$ , Equation 14 becomes

$$\frac{d^2x}{d\theta^2} + 2x = 0, \quad (15)$$

which has the solutions of  $x(\theta) = A \cos(\sqrt{2}\theta + \alpha)$ . Solving for  $A$  and  $\alpha$  requires applying the initial conditions. A full description of the mechanics of the analyzer would involve discussion of the trajectory given an entrance angle,  $\alpha$ , deviating from one tangential to

---

<sup>5</sup>The following derivation follows that found in Hughes and Rojansky (1929), [17].

<sup>6</sup>A derivation for Binet's Equation appears in Appendix I.

the curvature of the analyze, but because the case of  $\alpha = 0$  is sufficient for deriving the resolution, it is the case that will be explored here. The case of  $\alpha = 0$  is described by the initial condition:  $\frac{dy}{d\theta}(0) = 0$ . This condition requires that  $A\sqrt{2}\sin(\sqrt{2}(0) + \alpha) = 0$ , or  $\alpha = 0$ . Further, because the particle starts out at  $u = \sqrt{\frac{E}{E_0}}u_0$ , we want  $y(0) = \sqrt{\frac{E}{E_0}}$ . These conditions determine that the first order approximate solution to Equation 14 is:

$$y(\theta) = 1 + \left( \sqrt{\frac{E}{E_0}} - 1 \right) \cos(\sqrt{2}\theta). \quad (16)$$

By relating  $y$  back to  $r$ , using  $r = r_0\sqrt{\frac{E}{E_0}}\frac{1}{y}$ , it is found that the approximate solution for ion orbits in the charge exchange analyzer is given by:

$$r(\theta) = \frac{\sqrt{\frac{E}{E_0}}r_0}{1 + \left( \sqrt{\frac{E}{E_0}} - 1 \right) \cos(\sqrt{2}\theta)}. \quad (17)$$

The shape of this approximate solution for a range of energies in an analyzer set to select 100 eV ions is plotted in Figure 10. The solution exhibits features that one would expect. When  $E = E_0$ , the solution reduces to circular motion, with  $r(\theta) = r_0$ . For small deviations in energy, the orbits are nearly circular, while for larger energy deviations from  $E_0$ , the ions travel on trajectories that deviate even further from circular ones.

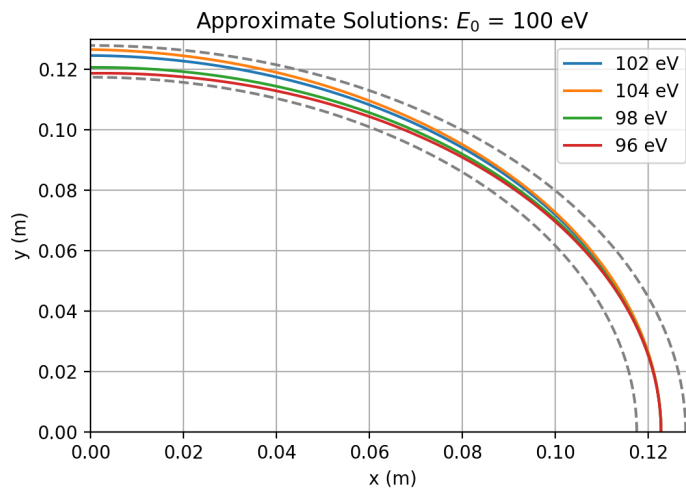


Figure 10: Approximate trajectories for energies near the selection energy when  $E_0 = 100$  eV.

To assess the accuracy of the approximate solution, a second-order forward Euler algorithm<sup>7</sup> is employed to solve Equation 14. If the differential equation is posed in the form:

$$y'' = f(y, t) = -y + \frac{1}{y}; \quad y(0) = \sqrt{\frac{E}{E_0}}; \quad \frac{dy}{d\theta}(0) = 0, \quad (18)$$

then the second-order Euler method finds the solution using:

$$y_0 = y(0); \quad y_1 = y_0 + \frac{dy}{d\theta}(0)\Delta t; \quad y_{n+1} = 2y_n - y_{n-1} + (\Delta t)^2 f(y_n). \quad (19)$$

Using the definition from above, that  $r = r_0\sqrt{\frac{E}{E_0}}\frac{1}{y}$ , one can find  $r(\theta)$  from the numerical solution for  $y(\theta)$ . Applying this iterative scheme for finding a numerical solution yields results that appear to be accurate and are in fact quite close to the approximate solution. The difference between the two trajectories is small, with the error, plotted in Figure 12, not exceeding a couple  $\mu\text{m}$ . For example, at the detector end of an analyzer ( $\theta = \frac{\pi}{2}$ ) set to 100 eV, the error for the trajectory of a 102 eV ion is only about 5 thousandths of a millimeter. In other words, the approximate solution should suffice for the regime relevant for the curved-plate analyzer.

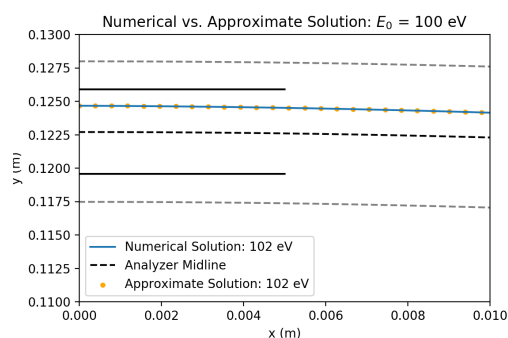


Figure 11: Plotting both numerical and approximate solutions at the detector end of the analyzer.

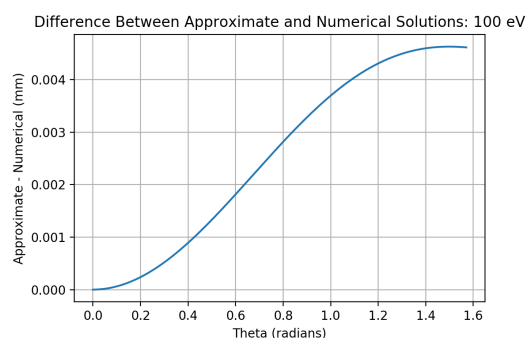


Figure 12: The difference between the numerical and approximate solutions. Angle step size is  $1.5 \cdot 10^{-5}$  radians.

By using the approximate solution for the motion of ions in the curved-plate analyzer, it is possible to approximate the resolution for a beam of ions entering the analyzer at the same point, i.e. the values of  $E$  for which  $r(\pi/2) \in (r_0 - \delta r, r_0 + \delta r)$ . Formulated

<sup>7</sup>Thank you to Prof. Mikko Haataja for his guidance on the topic of numerical solutions to ODEs. The algorithm comes from his lecture notes for MAE 306.

differently, the accepted energy range is  $\Delta E = E_+ - E_-$ , where  $E_+$  is the energy for which  $r(\pi/2) = r_0 + \delta r$  and  $E_-$  is the energy for which  $r(\pi/2) = r_0 - \delta r$ . The energy resolution,  $\Delta E/E$  is thus given by  $\frac{E_+ - E_-}{E}$ . Letting  $\alpha = \cos(\phi)$ , where  $\phi$  is the angle that the analyzer subtends, and solving for  $E_{\pm}$ , one finds that:

$$r_0 \pm \delta r = \frac{\sqrt{\frac{E_{\pm}}{E_0}} r_0}{1 + \left(\sqrt{\frac{E_{\pm}}{E_0}} - 1\right) \alpha} \rightarrow E_{\pm} = E_0 \left( \frac{\left(1 \pm \frac{\delta r}{r_0}\right) (1 - \alpha)}{1 - \alpha \left(1 \pm \frac{\delta r}{r_0}\right)} \right)^2. \quad (20)$$

By using  $\Delta E/E = \frac{E_+ - E_-}{E}$  from above, the energy resolution is given by:

$$\frac{\Delta E}{E} = \left( \frac{\left(1 + \frac{\delta r}{r_0}\right) (1 - \alpha)}{1 - \alpha \left(1 + \frac{\delta r}{r_0}\right)} \right)^2 - \left( \frac{\left(1 - \frac{\delta r}{r_0}\right) (1 - \alpha)}{1 - \alpha \left(1 - \frac{\delta r}{r_0}\right)} \right)^2 = f(\delta r, r_0, \alpha). \quad (21)$$

Although this expression is not simple, it only depends on three parameters: the width of the exit aperture ( $\delta r$ ), the radius of entry ( $r_0$ ), and the angle that the curved plates subtend ( $\alpha = \cos(\phi)$ ). Significantly, then, the  $\frac{\Delta E}{E}$  resolution is only a function of these three geometrical properties of the analyzer, leading to the fact that the accepted energy range  $\Delta E$  is linear in the energy, with  $f(\delta r, r_0, \alpha)$  as the slope, or  $\Delta E = f(\delta r, r_0, \alpha)E$ .

In papers reporting on similar analyzers, the figure of  $\frac{\Delta E}{E} = \frac{\delta r}{r_0}$  is often reported as the energy resolution [8]. The figure does not take into account the angular dependence of the analyzer for the resolution. The  $\frac{\delta r}{r_0}$  figure is the minimum possible resolution for the analyzer, but it only applies in the case of the  $\frac{\pi}{\sqrt{2}} \approx 127^\circ$  analyzer. For the analyzer in use in the SC-IEA, which subtends  $90^\circ$ , the resolution is expected to be slightly larger. The difference between Equation 21 and the oft-cited resolution is a slight one, with the more important result being that  $\Delta E$  is a linear function of ion energy.

To summarize the main results from this section, by modelling the curved plate analyzer as a cylindrically symmetric system, it is possible to derive a formula for the electric field between the plates (Equation 9). Using this formula for the electric field, it is possible to derive a formula for the proper voltage to apply to the plates in order to select for specific energies (Equation 11). By using Binet's Equation from the analysis of central fields, one can derive an approximate solution for the ion's trajectory through the curved-plate analyzer (Equation 17), which can be used to find a formula for the expected energy resolution of the analyzer (Equation 21). This theory for the operation

of the curved-plate analyzer is experimentally tested during calibration, described in Section 3.

## 2.3 Measurement of Analyzer Properties

From the above, it appears that if the theoretical model of the charge exchange analyzer is indeed correct, the proportionality factor between applied voltage and selected energy as well as the energy resolution of the analyzer are fully determined by the geometry of the system. From the measurements that were made in Summer 2021, the rough values of these geometrical properties are presented in the table below:

Quantity	Symbol	Value
Inner Plate Radius	a	11.75 cm
Outer Plate Radius	b	12.8 cm
Spacing Between Plates	d	1.05 cm
Aperture Width	$\delta r$	0.635 cm

By using these measurements and the model for the analyzer presented above, the proportionality factor between applied voltage and selected energy is 0.0856, i.e.  $V(E_0) = 0.0856 * E_0(\text{eV})$ , and the resolution is calculated using Equation 21 to be 6.44%.

Although these measurements seem to reveal a great deal about the operation of the analyzer, this method is nevertheless insufficient to rely upon experimentally. Experimental calibration of the system using a known ion source is necessary for two reasons. First, obtaining accurate measurements of the radii of curvature of the two plates is not so reliable. Finding the center of curvature is difficult, so the radius of curvature is difficult to measure accurately. Because the dependence of the proportionality factor is  $\ln(\frac{b}{a})$ , small mismeasurements in the radii of curvature lead to significant changes in the proportionality factor. For instance, if  $b$  in truth was only 1% higher and  $a$  was in truth one percent lower (an error of just 1.1 mm), the proportionality factor would be 0.106. If the error was in the opposite direction, the proportionality factor would be 0.656. Secondly, the differences between the physical model and reality may lead to differences in the values of the proportionality factor and the resolution. To illustrate, a host of factors not taken into account by the model may contribute to energy selection and resolution. The presence of fringing fields due to the fact that the plates do not form a full circle will cause the equation for electric field to only be an approximation, changing the resolution and energy selection. The lack of a perfect vacuum in the analyzer

will cause further scattering and spread of angles. Electromagnetic forces within the ion beam itself may change the dynamics of an ion's path through the analyzer. In short, there is a long possible litany of finer physical effects that will cause the experimentally observed phenomena to differ from the picture presented in this section. Including this list of possible effects on the resolution in our model would be impossible, so empirical determination through a physical calibration is a critical step in rendering the analyzer useful for the determination of the ion energy distribution.

## 2.4 Stripping Cell

The stripping cell serves as a method for ionizing the neutrals that exit the plasma so that they can be selected by energy in the curved-plate analyzer. The operating principle is that there is a certain fraction of the incoming neutrals will be ionized through collisions with neutral gas particles in the stripping cell. The model used in Adlam and Aldcroft (1969), [18], which is described in further detail below, allows for two other possibilities, collisions that cause neutrals to scatter out of the aperture path, and collisions that cause newly created ions to borrow an electron and return back to neutrals. This model is parameterized by three cross sections:  $\sigma_i$ ,  $\sigma_{EC}$ , and  $\sigma_s$ , which are the ionization cross section, the electron capture cross section, and the scattering cross section. Using these three parameters and given an initial flux of neutrals,  $H_0$ , one can write coupled differential equations for the neutral flux,  $\phi_H(x)$ , and the ionized flux,  $\phi_i(x)$ , as functions of position <sup>8</sup>:

$$\begin{aligned}\frac{d\phi_H}{dx} &= n\sigma_{EC}\phi_i - n(\sigma_s + \sigma_i)\phi_H \\ \frac{d\phi_i}{dx} &= -n(\sigma_s + \sigma_{EC})\phi_i + n\sigma_i\phi_H,\end{aligned}$$

where  $n$  is the density of neutral gas in the gas stripping cell. The solutions to these equations are found by forming two decoupled second-order ODEs and applying boundary conditions. The solutions are:

$$\phi_i(x) = H_0 \frac{\sigma_i}{\sigma_i + \sigma_{EC}} e^{-n\sigma_s x} \left( 1 - e^{-n(\sigma_i + \sigma_{EC})x} \right) \quad (22)$$

$$\phi_H(x) = H_0 e^{-n\sigma_s x} \left( 1 + \frac{\sigma_i}{\sigma_i + \sigma_{EC}} \left( e^{-n(\sigma_i + \sigma_{EC})x} - 1 \right) \right). \quad (23)$$

---

<sup>8</sup>The derivation for the efficiency follows that in [18].

Defining the efficiency of the stripping cell as  $\eta = \frac{\phi_i(l)}{H_0}$ , where  $l$  is the stripping cell length, it is found that:

$$\eta = \frac{\sigma_i}{\sigma_i + \sigma_{EC}} e^{-n\sigma_s l} \left(1 - e^{-n(\sigma_i + \sigma_{EC})l}\right). \quad (24)$$

The best pressure to run the system at is found by taking setting  $\frac{d\eta}{dn} = 0$  and solving for  $n$ . When this is done, it is found that:

$$n_{max} = \frac{1}{l(\sigma_i + \sigma_{EC})} \ln \left( \frac{\sigma_i + \sigma_{EC} + \sigma_s}{\sigma_s} \right), \quad (25)$$

which gives the density in particles/cm<sup>3</sup>. To convert this to a maximum pressure, the ideal gas law is used:  $PV = NkT \rightarrow P_{max} = n_{max}kT$ :

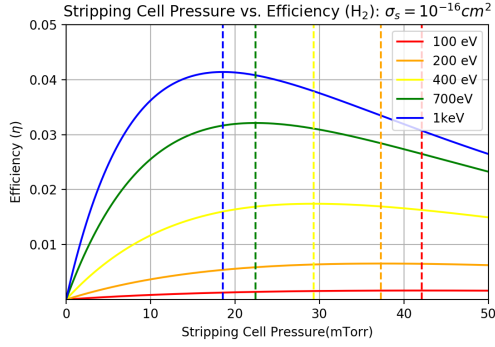
$$P_{max} = n_{max} \left( \frac{10^2 \text{cm}}{\text{m}} \right)^3 \left( 1.3806 * 10^{-23} \frac{\text{J}}{\text{K}} \right) (293 \text{ K}) \left( \frac{0.0075 \text{Torr}}{\text{Pa}} \right) \left( \frac{10^3 \text{mTorr}}{\text{Torr}} \right),$$

or,  $P_{max} = n_{max} (3.033 * 10^{-14} \text{mTorr} * \text{cm}^3)$ . The results are plotted using the following values for  $\sigma_i$  and  $\sigma_{EC}$ , taken from C. F. Barnett's measurements for hydrogen ions travelling through neutral hydrogen [19]. Because reactions depend on the ion's energy, the efficiency  $\eta$  is not a constant but rather is a function of ion energy,  $\eta(E)$ . The values for various ion energies are tabulated below.

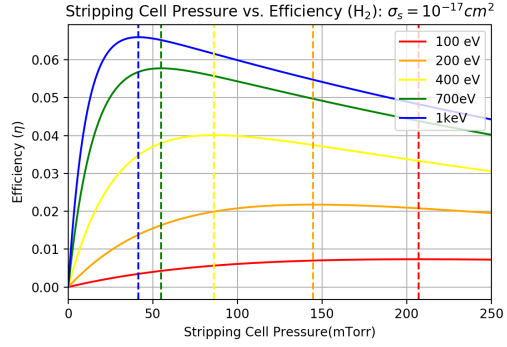
Energy (eV)	$\sigma_i$ (cm <sup>2</sup> )	$\sigma_{EC}$ (cm <sup>2</sup> )
100	$5.24 * 10^{-19}$	$3.65 * 10^{-17}$
200	$2.39 * 10^{-18}$	$6.96 * 10^{-17}$
400	$8.32 * 10^{-18}$	$1.56 * 10^{-16}$
700	$2.09 * 10^{-17}$	$2.93 * 10^{-16}$
1000	$3.37 * 10^{-17}$	$4.26 * 10^{-16}$

Because the scattering cross section is sensitive to the system's geometry, a range of possible values are used to illustrate roughly what the value of the pressure should be. The length used in plotting the pressure and efficiency is  $\approx 6$  cm, the length of the stripping cell.

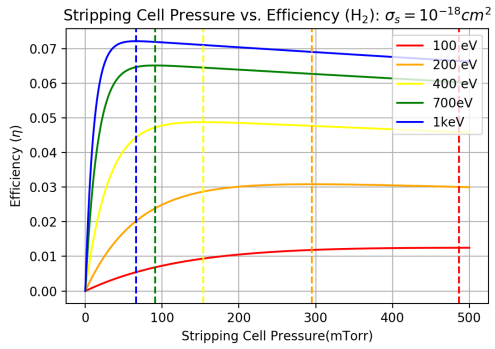
From Figure 11, it appears that the ideal pressure varies greatly based on the value of  $\sigma_s$ . When  $\sigma_s = 10^{-16}$  cm<sup>2</sup>, the ideal pressure is about 40 mTorr, to maximize the efficiency taking into account the various different energies. However, when  $\sigma_s = 10^{-19}$  cm<sup>2</sup>, the ideal choice is closer to 800 mTorr to maximize for the most values of ion



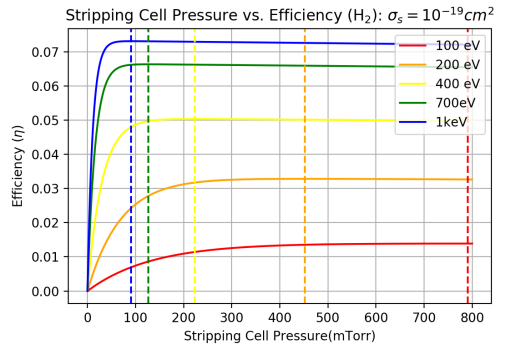
(a) Pressure vs.  $\eta(E)$  for  $\sigma_s = 10^{-16} \text{cm}^2$ .



(b) Pressure vs.  $\eta(E)$  for  $\sigma_s = 10^{-17} \text{cm}^2$ .



(c) Pressure vs.  $\eta(E)$  for  $\sigma_s = 10^{-18} \text{cm}^2$ .



(d) Pressure vs.  $\eta(E)$  for  $\sigma_s = 10^{-19} \text{cm}^2$ .

Figure 13: Plots of Pressure vs. Efficiency for various values of  $\sigma_s$  at different ion energies.

energy. Nevertheless, settling on a low pressure of about 40 mTorr for a slightly lower efficiency than the maximum for high energy ions is a fair plan, given that it ensures a high efficiency at high values  $\sigma_s$ .

A separate issue for the efficiency is that because the efficiency depends upon energy, it has the effect of shifting the relative abundance of energies to higher energies, because the efficiency grows with energy. Nevertheless, in the model presented, one can see that the efficiency always stays between about 1% and 10%, so it should not greatly influence the exponential tail of a Maxwellian from which temperature can be derived. In a non-Maxwellian distribution though, it would be best to develop a system, similar to the one described later for resolution, to filter out this skewing. Nevertheless, the change in the energy spectrum due to this effect will not be a great one and is one that can be accounted for.

To conclude, the value of  $\eta(E)$  was not experimentally determined during calibration, nor was the stripping cell tested, so stripping cell operation will be determined during the operation of the SC-IEA itself on the plasma device. Because  $\eta(E)$  was not experimentally tested, some uncertainty will be introduced in the ion energy distribution (IED), so future analysis of the IED will include the uncertainty in the IED reasonably contributed by the  $\eta(E)$  weighting of the stripping cell.

## 3 Calibration

This section will elaborate the process for the calibration of the SC-IEA, focusing on the process of gathering calibration data, the methods for analyzing the data, and the results found from the data. Along the way, the results are compared to those theorized in the previous section, both in terms of their overall qualitative behavior and the quantitative results. Carrying out calibration helped to clarify several aspects of the system, such as the relationship between the voltage on the plates and the ion selection energy, the resolution of the curved-plate analyzer, and the magnitude of the signal and its attenuation throughout the system. Analyzing the data helped pin down a value and error bars for the proportionality factor between plate voltage and ion energy, as well as roughly demonstrating that energy resolution,  $\Delta E/E$ , is constant as a function of ion energy. Both the proportionality constant and the resolution are measured to be different than the values found from direct geometric measurements that are entered into the theoretical model, a discrepancy discussed later in this section.

### 3.1 Procedure

Calibration of the curved plate analyzer was performed with an ion source of adjustable energy, the Physical Electronics Model 04-303 Ion Gun, obtained from Shota Abe in the Surface Science Laboratory at PPPL. The ion beam energy is adjustable from 0 eV to 5 keV with a precision of 10 eV. The goal of calibration was to set the ion beam energy to known values, vary the voltage delivered to the plates of the energy analyzer, and study the signal detected from the electron multiplier as a function of the voltage on the analyzer plates.

For the calibration process, two methods of applying voltage to curved plates were tested, direct current (DC) and alternating current (AC). The results from both methods are discussed in this section. The application of DC voltage was tested first, by using an HP-511 power supply. The positive and negative outputs of the power supply were both connected through resistors to ground to produce a positive and negative voltage of the same magnitude, as illustrated in Figure 14. This method was beneficial for the initial detection of a signal, which it will likely also be used for in the detection of initial data from the PFRC-2. However, because it did not allow for automatic variation of the voltage, building up enough data to determine a peak value with reasonable error took too long to allow for practical collection of data. Thus, the method for delivering voltage

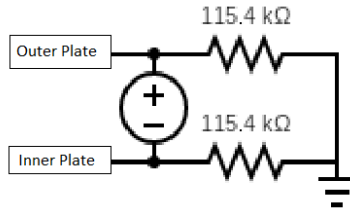


Figure 14: Circuit diagram for the DC voltage application.

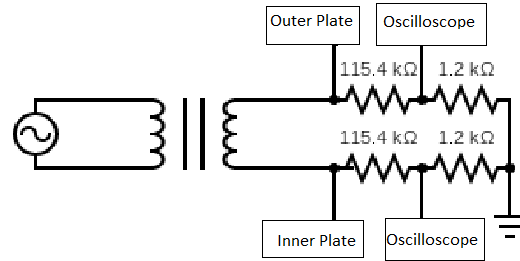


Figure 15: Circuit diagram for the AC voltage application.

that was used to collect data for the determination of the analyzer properties used an AC voltage source in the form of a Variac that was plugged into the wall. The voltage signal entered a transformer to be split into positive and negative signals around ground before being applied to the analyzer plates. The positive and negative voltages then passed through two resistors, one large ( $\approx 110 \text{ k}\Omega$ ) and one small ( $\approx 1.2 \text{ k}\Omega$ ), before both going to ground. Between the large and small resistors, the voltage was monitored by an oscilloscope so that the value of the applied voltage could be monitored and recorded to be matched with signal seen as a function of the applied voltage, as illustrated in Figure 15. When the SC-IEA is used on the PFRC-2, voltage delivery will be tested at higher frequencies by using a signal generator along with a bipolar operational amplifier in order to detect any anomalies or higher frequency physical phenomenon in the plasma that would be averaged out by using the relatively low frequency of 60 Hz coming from the wall.

To produce the data that was used for the determination of the analyzer properties, the signal vs. voltage were recorded at each energy for a large range of energies. For each of these energy data sets, the peak signal value was determined along with the peak width. By compiling the values of the peaks for each energy value and the standard deviations of the peak value for each energy, a reasonably linear fit is found, with the slope being the proportionality factor between applied voltage and the selected ion energy and the slope's error being the high and low limits for the proportionality factor. To determine the value of the energy resolution for the energy analyzer, the width of the energy peak at half maximum was taken to be the variance of the energy,  $\Delta E$ . These values for  $\Delta E$  are then divided by the energy,  $E$ , at each value to obtain a data set of  $\Delta E/E$  as a function of the ion energy.

Using a DC voltage signal, building up a full signal vs. voltage spectrum took a long time for data collection to be complete. At each voltage, the output of the electron multiplier had to be measured and the count rate recorded. The results are shown in Figure 16. The largest peak can be taken to be the selected energy peak. This method has two major problems. First, acquiring enough data to have a data set large enough

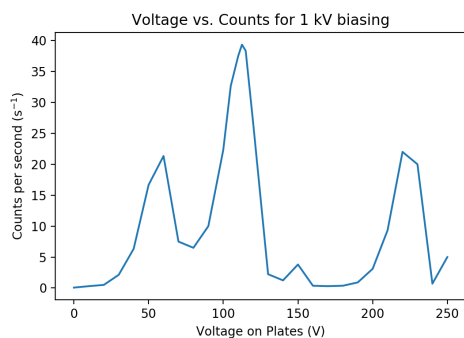


Figure 16: The voltage vs. signal for the DC voltage method.

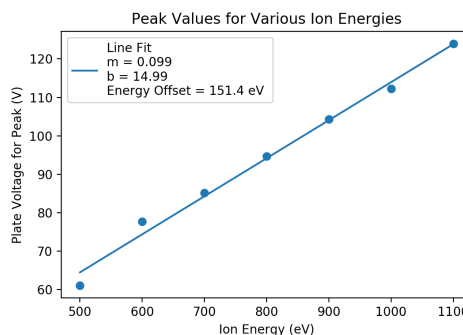


Figure 17: Ion energy vs. peak voltage with fitting line for the DC voltage method.

to determine the values of the proportionality factor between the voltage and energy with a reasonable uncertainty took too long. Second, the pressure in the ion gun is variable over the timescale for data collection over the whole voltage energy spectrum, so the count rate detected at lower voltages and higher voltages vary not only due to the energy difference in the ions being selected but also because of the pressure in the ion gun. Using an AC voltage signal remedies this problem by cycling through the whole voltage interval on a timescale much faster than the timescale for pressure to change in the ion gun. Rough as the DC method was, it demonstrated three significant features. First, as shown in Figure 16, there are clear peaks for which the signal was maximized at particular voltages, which is the expected behavior of the analyzer. Second, there appeared to be multiple peaks, a feature not predicted by the theory but one that was also observed by using the AC method. Third, by plotting and fitting the highest peak voltage values for different energies, the relationship between applied voltage and peak value appears to be a roughly linear one, shown in Figure 17. The value that was determined,  $\ln\left(\frac{b}{a}\right) = 0.099$ , was not an unreasonable deviation from  $\ln\left(\frac{b}{a}\right) = 0.0856$ , the value determined by the measurements of the analyzer's geometry.

The AC voltage method used a sinusoidal signal oscillating at the wall frequency of

60 Hz, a frequency far faster than the significant changes in count rate due to the varying pressure in the gas in the ion gun. An oscilloscope was used to trigger the signal from the electron multiplier at the same frequency as the voltage signal sent to the curved-plate analyzer. Thus, it was simple to plot the signal as a function of voltage delivered to the plates. In the data that was used, the signal was always given at least thirty seconds to accumulate an average.

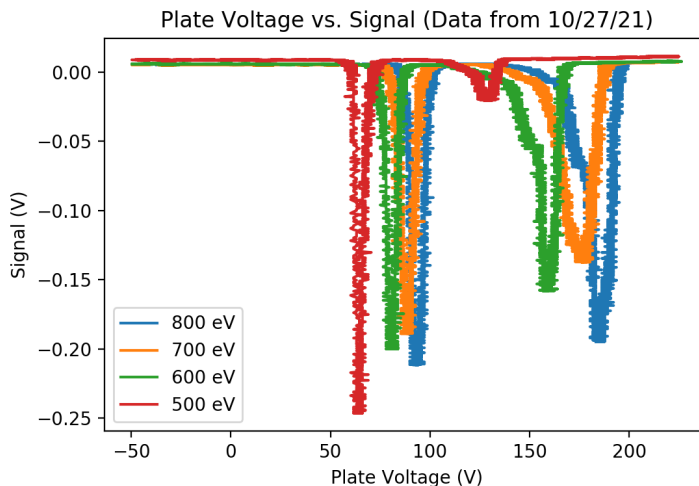


Figure 18: Data for voltage vs. signal taken for several energies using the sinusoidal voltage method.

Figure 18 shows several voltage vs. signal plots on the same graph. One can see that in each plot there are two sets of peaks that both vary as a function of the ion energy. As the energy grows, the peaks migrate to higher voltages. The symmetric peaks are closer to the expected energy based on the measurements, so the asymmetric peak population at higher voltages are treated as an anomalous peak.

Although the double peak problem was already evident from the DC voltage method, the peaks became even more clear by using the AC method. The determination is made due to two indications. First, the lower peak is at the voltage closest to that predicted by the measurements of the system geometry. Second, the higher peaks appear to be asymmetric, which is a feature not predicted for the energy peaks. There are several possibilities for the production of a second peak. The second peak does not appear to be due to a second ionization of the hydrogen ( $H_2$ ) molecules being pumped into the ion gun. Because the  $V(E_0)$  scales as  $q^{-1}$ , a higher ionization should result in peaks at lower

voltages, not higher voltages. Further, data taken with helium (He) as the ionization gas also demonstrated the same second peak, even though the difference in the ionization potentials of helium and hydrogen should present different peaks. Another possibility that appears to be unlikely is that the beam dislodges atoms from the probes in its path and causes them to speed up. This explanation seems unlikely because collisions with interposing material should dissipate the energy in the beam, as discussed in [8], not add energy. The most likely explanation for the extra peak is due to an internal operation due to focusing in the ion gun. By shifting the electrostatic lenses that focus the ion beam, the beam not only grows stronger and weaker, but the ratio of high peak to low peak also shifts, indicating that the second peak is likely due to the focusing mechanism of the ion gun, although further information is required in order to pinpoint the exact cause of this phenomenon.

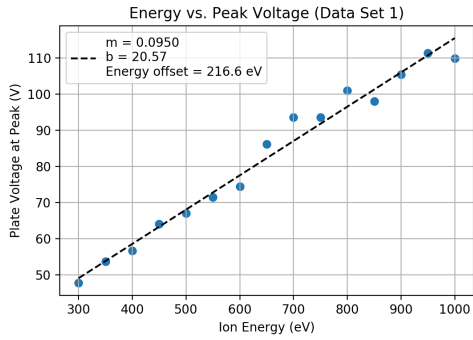
### 3.2 Results for the Voltage-Energy Relation

The calibration yielded reasonable values and errors for the proportionality factor as well as a general confirmation of the theoretical model for the energy resolution of the analyzer. Six sets of data were analyzed, shown in the graphs in Figure 19. Each set consists of the voltage at the signal peak as a function of energy for energies in the range of 200 eV - 1 keV. Ions with energy less than 200 eV were difficult to detect. The graphs each show the slope and y-intercept for the data set, calculated using Numpy's built-in polynomial fitting function. The "energy offset" is also displayed, a quantity defined later as  $\frac{b}{m}$ . These all seem reasonably precise with a mean of 0.0959 and a standard deviation of only 0.0028, a value only  $\approx 3\%$  of the mean.

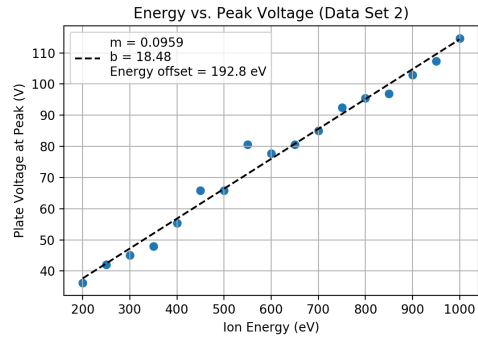
To come up with a different estimate that takes into account all of the data at once, the six data sets were combined to produce average values for the voltage for each energy value as well as the standard deviation from that value. The mean of the voltage ( $\bar{V}_i$ ) and the standard deviation ( $\sigma_i$ ) were calculated according to:

$$\bar{V}_i = \frac{1}{N} \sum_{j=1}^N V_{i,j}; \quad \sigma_i^2 = \frac{1}{N} \sum_{j=1}^N (V_{i,j} - \bar{V}_i)^2, \quad (26)$$

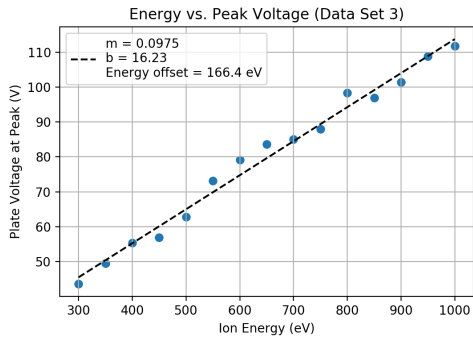
where N is the number of voltage measurements at each energy. In the present case,  $N = 6$ . The mean voltage value for each energy and its standard deviation (treated here as the error) are used to calculate the linear fit along with its error, as presented in



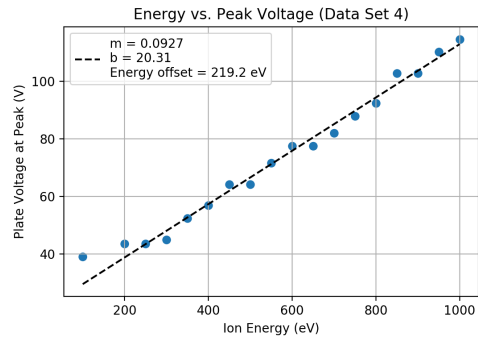
(a) Energy vs. Peak Voltage for Set 1.



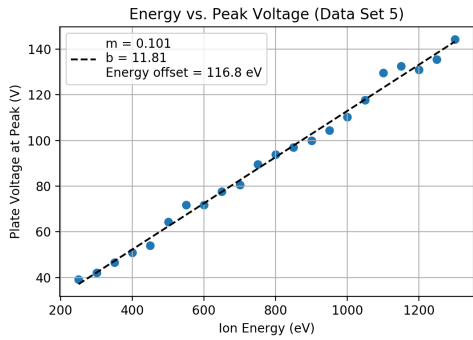
(b) Energy vs. Peak Voltage for Set 2.



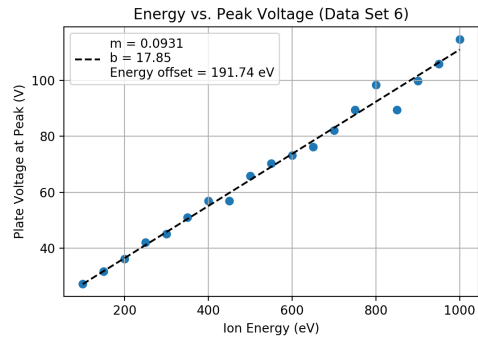
(c) Energy vs. Peak Voltage for Set 3.



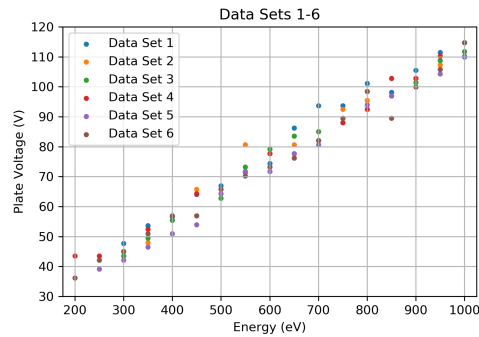
(d) Energy vs. Peak Voltage for Set 4.



(e) Energy vs. Peak Voltage for Set 5.



(f) Energy vs. Peak Voltage for Set 6.



(g) Data from all six data sets.

Figure 19: Figures for the proportionality factor between energy and voltage.

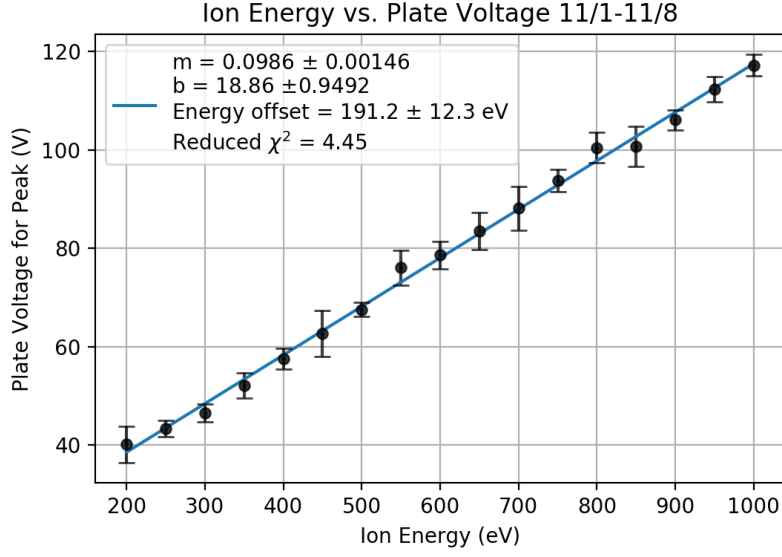


Figure 20: The final calibration results: Peak voltage vs. Energy with errors for energies between 200 eV and 1 keV.

Figure 20. The data in Figure 20 was then fit using a NumPy linear fitting function that returns the slope of the line as well as the error on the slope. To assess the plausibility of a linear fit, the reduced  $\chi^2$  is used:

$$\chi^2 = \sum_{i=0}^N \frac{(V_i - V_{fit})^2}{\sigma_i} \quad (27)$$

When the reduced  $\chi^2 \gg 1$ , the fit is a poor one, whereas when  $\chi^2 \ll 1$  the model is overfitted to the data. A reduced  $\chi^2$  of order unity shows a reasonable fit to the data. As shown from the reduced  $\chi^2$  for the data in Figure 20, which takes a value of 4.45, a value close to unity, the linear fit is a reasonable one.

One surprising feature that became apparent from plotting and fitting the data is the nonzero y-intercept. Based on the theoretical model for  $V(E_0)$  mentioned above, the y-intercept should be zero. This y-intercept is likely due to an offset in the ion beam energy. For example, if  $E' = E + E_0$ , then:

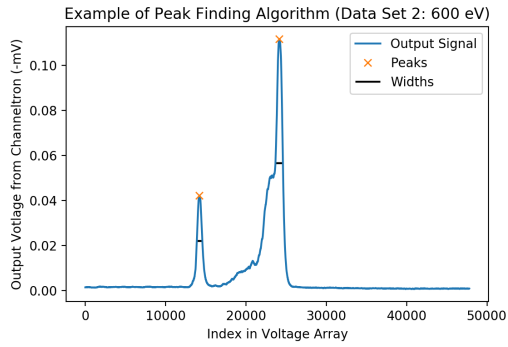
$$V(E') = \ln\left(\frac{b}{a}\right) E' = \ln\left(\frac{b}{a}\right) (E + E_0) = \ln\left(\frac{b}{a}\right) * E + \ln\left(\frac{b}{a}\right) E_0 \quad (28)$$

Thus, the energy offset should be given by  $\ln\left(\frac{b}{a}\right) E_0$ . As pointed out by Dr. Abe, a switch at the back of the ion gun was turned to “200 eV” ionization energy, which seems to produce the ions at a potential of 200 V. When the beam then travels to the center of the analyzer at a potential of 0 V, the ions gain 200 eV in energy. A natural test of the validity of the theory is if the y-intercept divided by the slope is close to the expected value of 200 eV. Indeed, for the data in Figure 20, this is the case, as the energy offset calculated from the six data sets used for the proportionality calculation is  $191.2 \pm 12.3$  eV, which is reasonable if the expected value for the offset energy is 200 eV.

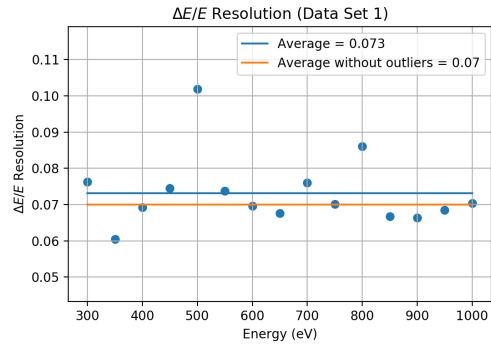
To summarize, the results from the calibration for the proportionality factor indicate that the trend between energy and voltage peak is linear. The proportionality factor between voltage and energy is  $0.0986 \pm 0.00146$  using the second method and  $0.0959 \pm 0.0028$  using the first method, where  $E_0$  is measured in eV. The two methods of extracting the proportionality factor overlap in the range of  $[0.0971, 0.0987]$ . The proportionality factor calculated based on the measurements of geometry was 0.0856, so the measured proportionality factor is within a reasonable range, especially because small deviations in the measurement of the curved plate radii greatly affect the proportionality factor between applied voltage and selected energy.

### 3.3 Results for the Resolution

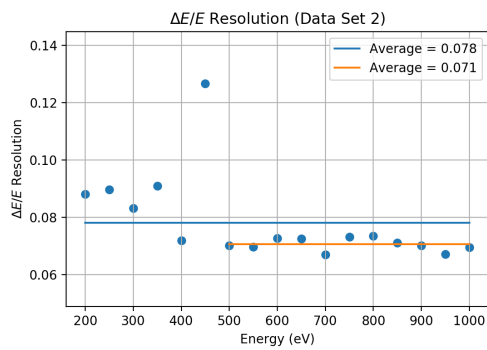
To determine the  $\frac{\Delta E}{E}$  resolution, the output of the Channeltron is simply passed through a python peak-finding algorithm (Scipy). The function determines the width of the peak at half of its maximum (FWHM), which is then divided by the energy of the peak. This quantity is taken to  $\Delta E/E$ . Because a sinusoidal voltage signal was used to deliver voltage to the curved-plate analyzer, The peak finding algorithm returns the position of the peak as the index of the voltage array. Because the energy of the peak is proportional to the voltage delivered to the analyzer, it is also proportional to the index of the voltage array, with the  $V = 0$  counting as the first index. Thus,  $\Delta E/E$  for the peak can just be taken to be the width of the peak in indices divided by the index of the peak starting from  $V = 0$ . The width of the peak used in calculating  $\Delta E/E$  is the FWHM of the peak, as illustrated in Figure 21a. The calculation of peak width is illustrated in Figure 21a. As discussed earlier, there is the issue of the presence of a second, asymmetric peak, at higher voltages, but for the calculations of the calibration factor and the resolution, only the first peak is used.



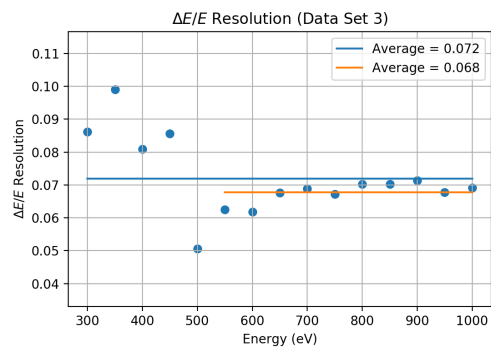
(a) Example of peak-finding algorithm.



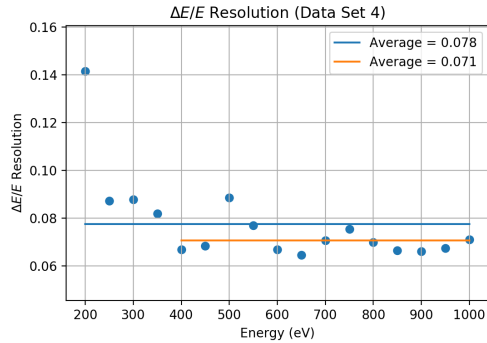
(b)  $\Delta E/E$  from Data Set 1.



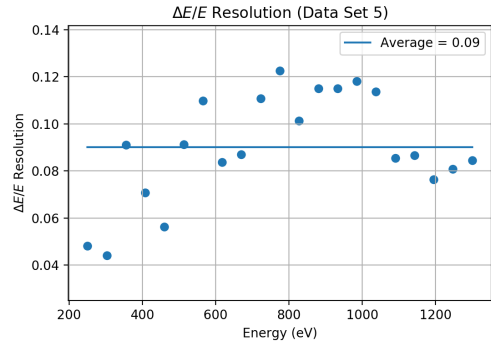
(c)  $\Delta E/E$  from Data Set 2.



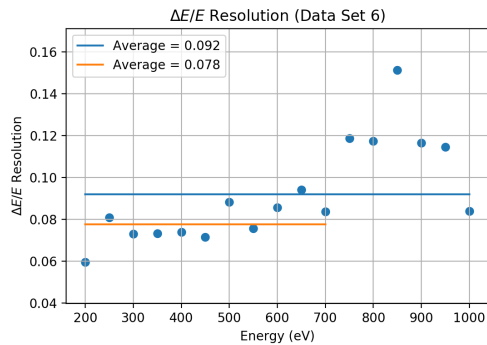
(d)  $\Delta E/E$  from Data Set 3.



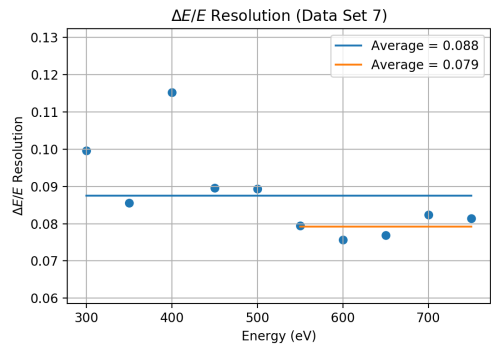
(e)  $\Delta E/E$  from Data Set 4.



(f)  $\Delta E/E$  from Data Set 5.



(g)  $\Delta E/E$  from Data Set 6.

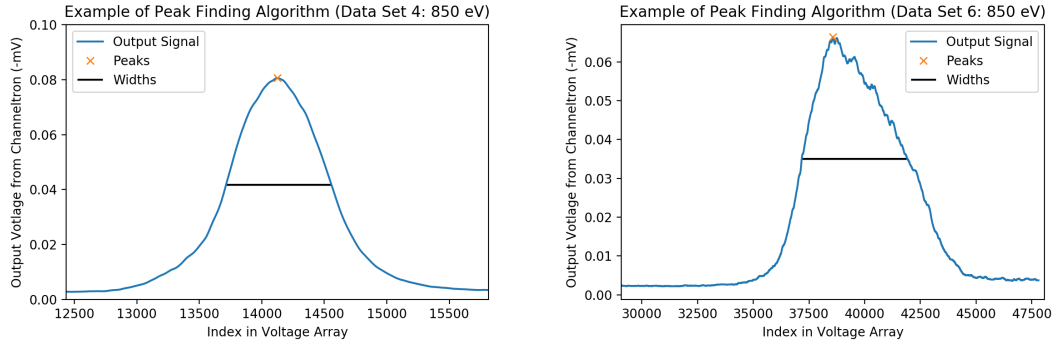


(h)  $\Delta E/E$  from Data Set 7.

Figure 21: Figures relating to the resolution.

The calculation described above was performed for each of the data sets from the calibration of the analyzer using the ion gun, with the results presented for each of the seven data sets in Figure 21 as graphs showing  $\Delta E/E$  as a function of energy.

Six out of seven of the graphs, i.e. all except for Figure 21f, do show that  $\Delta E/E$  is roughly constant over a significant portion of the energy range. Of those six graphs, only Figure 21b shows more or less constant behavior throughout the whole energy range, while the other five show a clear pattern in their variations from the constant baseline resolution. In Figures 21c, 21d, 21e, and 21h the resolution is higher at lower energies before falling to nearly constant values for energies higher than around 400 or 500 eV, while Figure 21g shows the opposite behavior where it appears that the resolution takes on a constant value for lower energies before rising to higher values for higher energies. This opposite behavior is probably due to some peculiar feature of the data collection, as the peaks that contribute to the abnormally large  $\Delta E/E$  values have asymmetric, jagged shapes. To illustrate, Figure 22 shows two peaks at equal energies, one from Data



(a) Symmetric peak from Data Set 4.

(b) Jagged peak from Data Set 6.

Figure 22: Figures illustrating peak width variation for the same energy.

Set 4, which has a constant  $\Delta E/E$ , and the other from Data Set 6, which has a widely varying  $\Delta E/E$ . Figure 22a, which has a resolution fitting with a broader constant trend, exhibits a symmetric peak, while Figure 22b, which is part of the non-constant trend in Data Set 6, has an abnormally shaped, asymmetric peak, demonstrating that the peak shapes in Data Set 6 are likely corrupted, perhaps as a result of varying voltage such that the data includes peaks of several energies. Specifically, in Data Set 6 the amplitude of the sinusoidal signal was varied for certain energies, to keep the peak energy near the top of the sinusoidal voltage. If data from the adjustment period of the plates was

included, or if the plates took longer than expected to adjust to a new voltage, then the energy acceptance of the peak would be broadened. The two data sets that exhibit the asymmetric peak shape were the two data sets in which the amplitude of the voltage signal was altered, perhaps leading to a similar asymmetrizing of the peaks.

The behavior seen in the group of five graphs with the behavior of poor resolution (higher  $\Delta E/E$ ) at low energies before cutting to constant resolution at higher energies remains the dominant behavior. This behavior requires explanation as it differs from the theoretically predicted behavior that  $\Delta E/E$  should be constant as a function of  $E$ . A similar behavior to this, along with two explanations, is reported in Beiersdorfer (1987), [8], in which  $\Delta E/E$  appeared to be largely constant at higher energies but grew with lower energies. First, the presence of fringing fields causes poorer resolution for low energies. Fringing fields will cause some additional energy in the radial direction, effectively causing a deviation in the entrance angle. For lower energy ions, the deviation in entrance angle is greater than for higher energy ions. To illustrate, the ion will gain some velocity  $v_r$  and  $v_\phi$  due to the fringing fields. The ion's entrance angle into the analyzer is given by  $\alpha = \arctan(\frac{v_r}{v_\phi})$ . Because the contribution to  $v_r$  will be a small contribution which is independent of ion energy, the ratio of  $\frac{v_r}{v_\phi}$  will be small for ions that begin with a high  $v_\phi$ , i.e. higher energy ions, and will be larger for ions that begin with a low  $v_\phi$ , i.e. lower energy ions. The second possible explanation for the data showing poorer resolution at lower energies could be due to the higher scattering cross section for ions of lower energy. Ions with lower energy could lose or gain slight amounts of energy through collisions with neutral gas particles in their path, leading to a broadening of the energy peak because there is, indeed a broadening of the energies. To test the plausibility of the first explanation, one needs to consider the predictions for the entrance angle. What fraction of the population will enter the analyzer at an angle, and how large is the fringing field expected to be? To test the second explanation, it is necessary to consider the likelihood of energy-altering collisions for incoming ions.

To pinpoint a value based on the figures above, by considering the constant regions in the five figures mentioned above,  $\Delta E/E$  takes a mean value of 7.2% with a standard deviation of 0.4%, so  $\Delta E/E \in [0.068, 0.076]$  when  $E$  is above  $\approx 400$  or  $500$  eV. This value is within reason for the analyzer, considering that the theoretical estimate based on measurements of the radius of curvature, aperture width, and angle subtended by the detector came out to be 6.44%.

However comforting this measurement may be in terms of its proximity to the

theoretical estimate, its narrow applicability in the energy range of interest may be a major hindrance in using it in practice. The range at which this value for  $\Delta E/E$  is relevant is the tail end of what the SC-IEA is expected to measure in the PFRC-2. To get a simple estimate for the resolution for energies below 450 eV, the resolutions for that range are averaged together, with their standard deviation serving as the uncertainty in the measurement. Because of the significant uncertainty for the resolution in this energy range, it is important to see how this range of  $\Delta E/E$  values may influence aspects of the observed signal, most importantly, its temperature,  $T$ . The standard deviation from the energies between 200 and 450 eV is about 1.2 %, so the reasonable values of  $\Delta E/E$  within two standard deviations are  $\Delta E/E \in [0.058, 0.106]$ .

### 3.3.1 Applying Resolution to Real Signals

In a real signal, because of the  $\Delta E/E$  resolution, in which the window of energy acceptance depends linearly on energy, the signal will appear to be shifted towards higher energies. This section will lay out the framework necessary to handle this energy-dependent  $\Delta E$ , along with an assessment of the effects that uncertainty in the value of  $\Delta E/E$  may have on the calculation of ion energy in the observed signal.

First, to illustrate the effects that the  $\Delta E \propto E$  resolution has on the signal, the effects are calculated for a plasma with a general energy distribution,  $f(E)$ . Discussion about the specific methods for handling the Maxwellian distribution are discussed a bit later. Because of the finite resolution, the signal at each energy  $E_i$  is really the integrated signal from energies  $E \in [E - \Delta E/2, E + \Delta E/2]$ . Therefore, if this distribution is sampled at energies  $E_i$ , then the corresponding signal  $g(E_i)$  that will be observed is given by:

$$g(E_i) = \int_{E_i - \Delta E/2}^{E_i + \Delta E/2} f(E) dE = \int_{E_i(1 - \frac{r}{2})}^{E_i(1 + \frac{r}{2})} f(E) dE, \quad (29)$$

where  $r = \Delta E/E$ . This same property can be exploited to produce a simple approximate routine for recovering the underlying energy distribution from the observed signal  $g(E_i)$ . If the integral in Equation 29 is approximated using the trapezoidal rule, which will be valid for small enough  $\Delta E$ , then the operation can be easily reversed without knowing the underlying distribution in advance. To illustrate, Equation 29 can be written

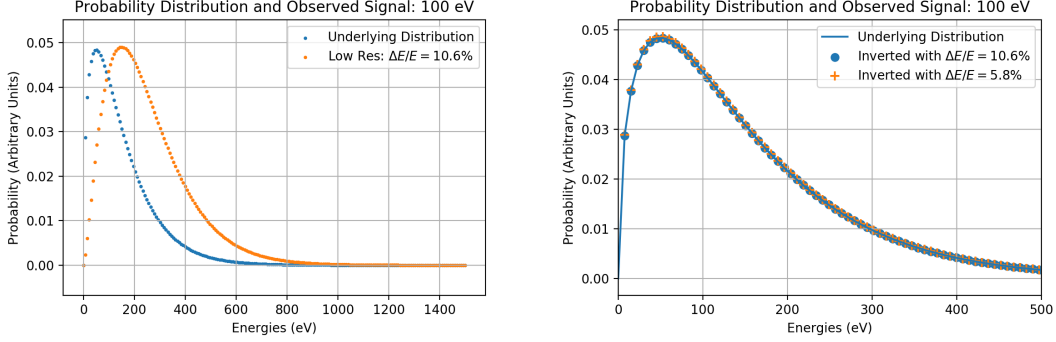
approximately as:

$$g(E_i) = \int_{E_i(1-\frac{r}{2})}^{E_i(1+\frac{r}{2})} f(E)dE \approx \frac{f(E_i(1+\frac{r}{2})) + f(E_i(1-\frac{r}{2}))}{2} rE_i. \quad (30)$$

By further approximating the integral by assuming that  $f(E_i(1+\frac{r}{2})) + f(E_i(1-\frac{r}{2})) \approx 2f(E_i)$ , it can be stated that:

$$g(E_i) \approx f(E_i)rE_i \longrightarrow f(E_i) \approx \frac{g(E_i)}{rE_i}, \quad (31)$$

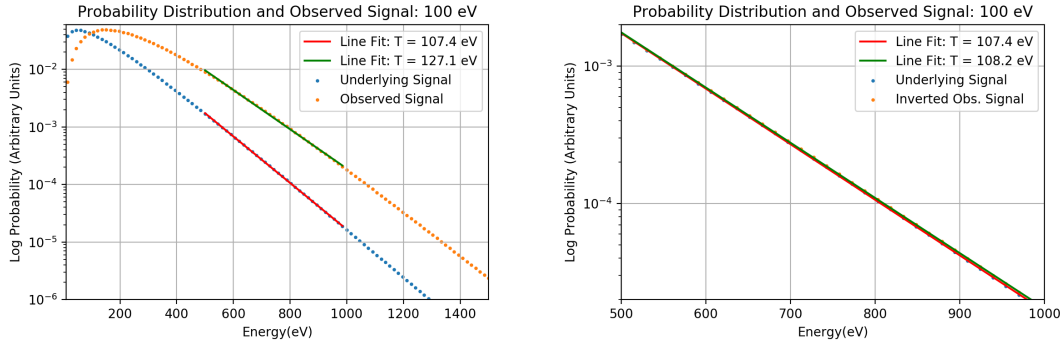
which is an approximation to the values of the underlying signal  $f(E_i)$  given an observed signal  $g(E_i)$  and the knowledge that the signal is observed through a resolution that depends linearly on energy.



(a) A Maxwellian distribution for  $kT = 100$  eV along with an observed signal assuming the underlying distribution using the technique that  $\Delta E/E = 0.106$ . (b) Inverting the observed signal to reveal eV along with an observed signal assuming the underlying distribution using the technique described in Equation 31.

Figure 23: Figures illustrating peak width variation for the same energy.

Figure 23a displays what may be the observed signal given an underlying distribution which is Maxwellian, defined as  $f(E) = 2E^{1/2}(\pi T^3)^{-1/2}e^{-E/kT}$ . The orange curve is the observed signal, which has been weighted using  $\Delta E \propto E$  such that it is shifted towards higher energies. The method for correcting for this shifted weight described in Equation 31 is illustrated in Figure 23, in which the “observed signal” from Figure 23a is inverted back to the “underlying signal” according to Equation 31. To reflect the uncertainty in the actual value of  $\Delta E/E$ , especially at lower energies, the method is implemented using the two farthest values that  $\Delta E/E$  is likely to take. In Figure 24a, one can see that the inversion scheme produces an underlying signal almost identical to the



(a) A Maxwellian distribution for  $kT = 100$  eV along with an observed signal assuming the underlying distribution using the technique that  $\Delta E/E = 0.106$ . (b) Inverting the observed signal to reveal the underlying distribution using the technique described in Equation 31.

Figure 24: Figures illustrating peak width variation for the same energy.

original one, despite the crude assumptions made in inverting the process of integration that takes place during signal collection. Furthermore, the inversion scheme described in Equation 31 does not really depend on the value of  $\Delta E/E$  because  $r$  acts only as a scale factor in the equation. The use of more sensitive integration techniques than the trapezoid rule would depend more significantly on the value of  $r$ .

If the distribution is Maxwellian, the temperature can be inferred by looking at the tail of the distribution. In this case, the inversion scheme is very accurate, returning almost the same temperature that would be inferred from the Maxwellian itself. Figure 22 illustrates the calculation of the temperature of the Maxwellian using a line fitting scheme to the tail end of the distribution. This is performed by taking the natural logarithm of the distribution, i.e., according to:

$$\ln(f(E)) = \ln(A) + \frac{1}{2} \ln(E) - \frac{E}{kT}, \quad (32)$$

which, because  $\ln(E)$  grows much more slowly than  $E$ , can be approximated for large  $E$  as:

$$\ln(f(E)) \approx -\frac{1}{kT}E + B. \quad (33)$$

The slope of this line is  $-\frac{1}{kT}$ , so one can find the temperature of the distribution by taking  $kT = -\frac{1}{\text{slope}}$ . In the figures above, the Maxwellian has a characteristic temperature of 100 eV, and calculating the temperature using a linear fitting for the natural logarithm of the signal recovers that temperature fairly accurately. Applying Equation 33 to the

“underlying” and “observed” signals in Figure 24a, for instance, yields temperatures of 107.4 eV and 127.1 eV, respectively. By inverting the “observed signal,” the temperature measured from the “observed” signal is much closer to the “underlying signal” at 108.2 eV. The result from this inversion is shown in Figure 24b. Thus, if the underlying signal is a Maxwellian, then applying even a crude inversion process can recover the temperature to within 1% of what the temperature would have been measured using the underlying signal. Further, from Figure 23b it can be seen that the inverted signal itself is quite close to the original. Therefore, to answer the question posed earlier, the large uncertainty in the resolution for energies below  $\approx 450$  eV is unlikely to pose a significant obstacle to the accuracy of the data analysis. Nevertheless, the calculation of the resolution from calibration data is a helpful confirmation that, at least at high enough energies, the resolution is roughly a linear function of energy.

### 3.4 Magnitude of the Signal on the Channeltron

Aside from calculating the proportionality between energy and voltage or the value of the analyzer’s energy resolution, another goal of calibration was the measurement of the current variation as it travels through the port crosses before it finally enters the curved-plate analyzer. The current was measured using the two current probes, which were bare metal wires connected to picoammeters inserted into the path of the beam. The probes were designed by Bruce Berlinger to be able to rotate in and out of the path of the beam while maintaining a tight vacuum seal. The two probes interfered with the beam in ways that were unexpected. For instance, moving the probes in or out of the path sensitively influenced the amount of signal seen exiting the Channeltron. Specifically, the presence of Probe 1 in the path of the beam increased the amount of signal seen, while barely any signal was seen without the probe in the path. The source of this phenomenon is not particularly clear, but it may have to do with the wire focusing the beam in some way. Especially considering the possibility that the beam exits the ion gun at some offset positive voltage, the presence of a floating potential wire may effect the signal before it reaches the 0 V midline of the curved-plate analyzer.

From the data in Figure 25, it appears that the current is attenuated by a factor of about  $\frac{1}{60}$  as it passes through the stripping cell. There appears to be sharp cutoff in the transmission of current between 700-800 eV. Until 700 eV, the current is attenuated by about a factor of  $\frac{1}{60}$  while for higher energies, the attenuation factor is closer to  $\frac{1}{1000}$ . The reason for this cutoff is not so clear. On the contrary, the main two expected con-

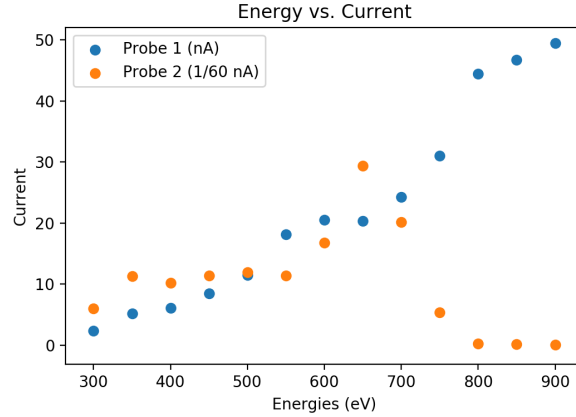


Figure 25: The current on both probes as a function of ion energy. Probe 1 is the probe closest to the ion gun.

tributions for attenuation, collisions with gas molecules and angular divergence, should lead to attenuation that decreases with energy or stays constant with energy, respectively. One possible explanation could have to do with some cutoff in how the beam is focused for higher energy ions in such a way that leads to a decrease of current in the second probe, although this requires further investigation.

One of the outstanding problems observed during the calibration of the SC-IEA with the ion source was the gap between the current of the observed signal at the Channeltron detector and the current as measured at the probes. Although the count rate at the electron multiplier was not recorded directly, for energies lower than a keV, there were not more than a couple pulses per period. Because the frequency of the applied voltage on the curved-plate analyzer was 60 Hz, if there were 5 counts per period, this would be a flow of about 300 ions/s. Although this number is very rough, it provides a rough number to compare to the current seen from the ion gun on the second probe. However this is significantly lower than the current seen in the second probe. For instance, the current seen at the second probe for ions of 500 eV was 0.2 nA, or:

$$0.2\text{nA} = 2 * 10^{-10} \frac{C}{s} * \left( \frac{H^+}{1.602 * 10^{-19} C} \right) \approx 1.25 * 10^9 \frac{\text{ion}}{s}, \quad (34)$$

about a billion ions per second, which is 7 orders of magnitude higher than what roughly was observed.

There are several considerations that may lead to a reduction in the current. First,

it is reasonable to assume that the 1/60 attenuation experienced between the first and second probe is repeated between the second probe and the Channeltron. Second, because the voltage signal applied to the curved-plate analyzer is sinusoidal, the analyzer only spends a limited amount of time at voltages that can accept the selected ion energies. Finally, if some of the ions enter at a non-zero entrance angle, they may be excluded from detection. The rest of this section will quantify the final two considerations to test their contributions to beam attenuation.

The second consideration in the reduction of current from the second probe to the curved-plate analyzer is the fraction of each period spent at a voltage that can collect the target energy. As discussed earlier, because of the nonzero aperture width, there is an energy resolution  $\Delta E/E = r$ , i.e. an energy  $E_0$  is accepted when the voltage takes values between  $V(E_0(1 + \frac{r}{2}))$  and  $V(E_0(1 - \frac{r}{2}))$ . In the case of the calibration, the applied voltage function was:

$$V(t) = A * \sin(f * t), \quad (35)$$

so the amount of time per period spent collecting a particular energy  $E_0$  is given by:

$$T_{total}(E_0) = \frac{1}{f} \arcsin\left(\frac{V(E_0(1 + \frac{r}{2}))}{A}\right) - \frac{1}{f} \arcsin\left(\frac{V(E_0(1 - \frac{r}{2}))}{A}\right). \quad (36)$$

Equation 36 is evaluated in Figure 26 for a  $\Delta E/E$  resolution of 0.1, a quantity slightly larger than that the range experimentally determined in the previous section. The other parameters in Equation 36 are used the measured quantities of the analyzer reported in Section 2.3. Figure 27 plots this time as a fraction of the total period, i.e. the fraction of each period spent collecting energy  $E_0$ .

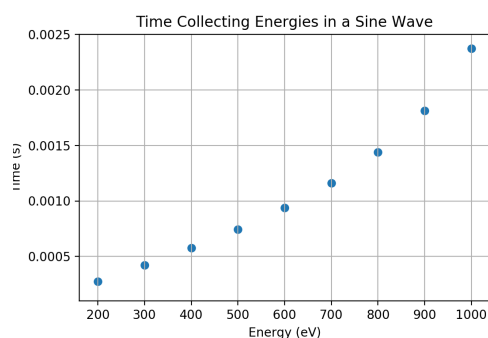


Figure 26: The total time in one period spent at each energy,  $E_0$ .

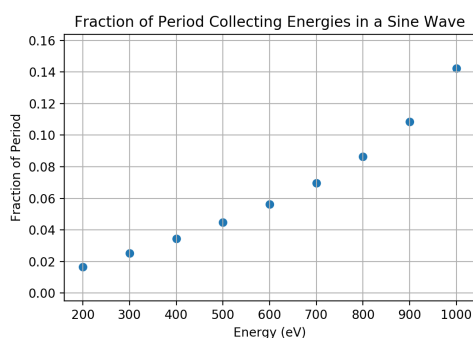


Figure 27: The fraction of a period spent at each energy,  $E_0$ .

From the above, one can see that the fractional amount of each period spent at the target energy will attenuate the amount of current delivered to the Channeltron. For a 500 eV electron during calibration, there was only 0.74 ms of collection time per period, or 4.4% of each period. Thus, we can use an attenuation factor of  $\approx \frac{1}{25}$  for this cause of reduction.

Another consideration that might have been entertained for why the current is attenuated is that ions entering the curved-plate analyzer have a large enough angle to prevent their passage through the curved plates. However, this consideration does not lead to a reduction of current when the relevant angles in this situation are taken into account. Because the stripping cell aperture is  $\approx 0.1$  inches, and the length of the first portcross is  $\approx 20$  inches, the largest angle allowed to exit the stripping cell is  $\theta = \arctan(0.1/20) = 0.28^\circ$ . Thus, the widest possible range of angles into the curved-plate analyzer is  $\theta \in [-0.28^\circ, 0.28^\circ]$ . However, even if an ion entered the analyzer at an angle of  $0.28^\circ$ , it would likely still reach the Channeltron.

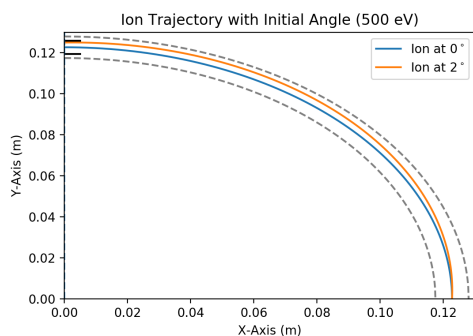


Figure 28: Simulated trajectories of two ions at 500 eV through the detector, marked in dashed gray lines.

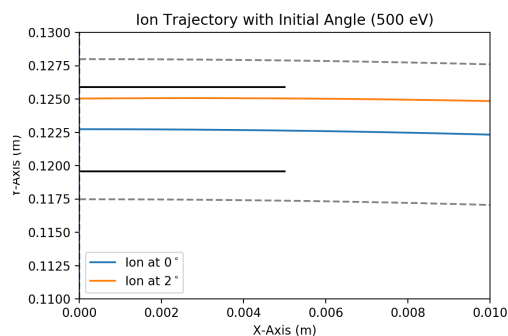


Figure 29: The two trajectories in Figure 28 seen in closeup as they enter the exit aperture.

Figures 28 and 29 show the trajectories of two ions at 500 eV, with one entering the curved plates tangential to the analyzer's curvature ( $\alpha = 0^\circ$ ) and one at an angle of  $2^\circ$  relative to the analyzer plates' curvature. Both ions safely enter the exit aperture and continue into the Channeltron. If an ion oriented at  $2^\circ$  still passes through the analyzer, than an ion at a tenth of that angle will likely exit the aperture as well, even though the simulation is based on non-ideal measurements of the curved-plate analyzer, as elaborated upon in the section discussing the calibration of the curved-plate analyzer.

Applying the two further reduction factors accounts for a total reduction of  $\frac{1}{1500}$ , or a total incoming current expected to be  $8.3 * 10^5 \frac{\text{ion}}{\text{s}}$ , which is now about 2000 times the magnitude of the “observed” current of 300 ions per second. The result of the remaining discrepancy is unclear.

The current may be further reduced because the pressure in the portcross from Probe 2 to the curved plates is approximately twice that of the portcross housing Probe 1. This may mean that the reduction factor between Probe 2 and the curved plates is  $\approx \frac{1}{120}$  as opposed to  $\frac{1}{60}$ . Nevertheless, this would mean that the observed current is still about 1000 times less than what would be expected, so for now, the reason for the magnitude of the current remains unclear.

To summarize this section, calibration using the known-energy ion source allowed for an experimental determination of the validity of the theoretical expectations of the curved-plate analyzer. The relationship between plate voltage and ion energy was determined to be linear as expected, and the resolution was determined to be mostly constant at higher energies, with a larger spread and tendency toward lower resolution at lower energies. The magnitude of the signal was measured at the two probes, although it is hard to justify the low current entering the Channeltron.

## 4 Installation on the PFRC-2

This section will discuss the plans for the connection between the SC-IEA and the PFRC-2 plasma device. The desired properties of the connection will be discussed as well as the plans to implement them.

### 4.1 Port and Tubing Design

To construct the connection between the SC-IEA and the vacuum vessel, the connecting pipes, the angle relative to the vacuum vessel, and the lengths need to be specified. The desired capabilities of the connection are the ability to view the neutral flux from various angles relative to the midplane and minimizing the attenuation of neutral flux because of the connection angles. As mentioned above in the introduction, the PFRC-2 can be thought of as an axisymmetric device, with three main directions, the  $\hat{z}$ ,  $\hat{r}$ , and  $\hat{\theta}$  directions. The synthetic diagnostic (SD) module on the RMF code predicts that neutrals exiting the vessel will likely not be purely radial; rather, they will exit at some angle  $\theta_0$  due to nonzero velocity in the  $\hat{z}$  direction, i.e. in the direction of the major axis. Further, this angle could depend on the specific parameters used to run the plasma. The design of the pipe connecting the diagnostic to the vessel accounts for this by using a bellows that can bend. Further, the pipe inserted in the vessel is done so at an angle in the first place.

Once the observation angle is set, there is a very small angular resolution due to the length of the diagnostic and the small aperture at the end of the diagnostic. Specifically, the angular resolution is:

$$\theta = \arctan\left(\frac{l}{d}\right) = \arctan\left(\frac{40}{0.25}\right) = 0.35^\circ, \quad (37)$$

so whatever angle  $\theta_0$  the detector is set to, the effective angles seen will be between  $\theta_0 - 0.35^\circ$  and  $\theta_0 + 0.35^\circ$ , although larger angles may exist due to scattering along the ion path as well.

To implement these desired capabilities, the installation on the vacuum vessel consists of two distinct parts, a primary 2.25" polycarbonate tube penetrating the vessel itself and then a 6 inch stainless steel bellows that connects the tube and the diagnostic. The polycarbonate tube allows for the neutrals to move towards the diagnostic past the copper antennae, while the bellows allows for adjustment of the angle between the

diagnostic and the machine to enable detection of the flux at different angles relative to the midplane.

To allow for minimal attenuation of the flux, the bellows should be curved as little as possible. This is because the bellows does not redirect the flux, it simply reorients the diagnostic to look at an angle. In doing so it lowers the effective flux seen by the diagnostic. Hence, it is best to place the tube at an angle into the vacuum vessel itself, so that flux at the desired angles is greater.

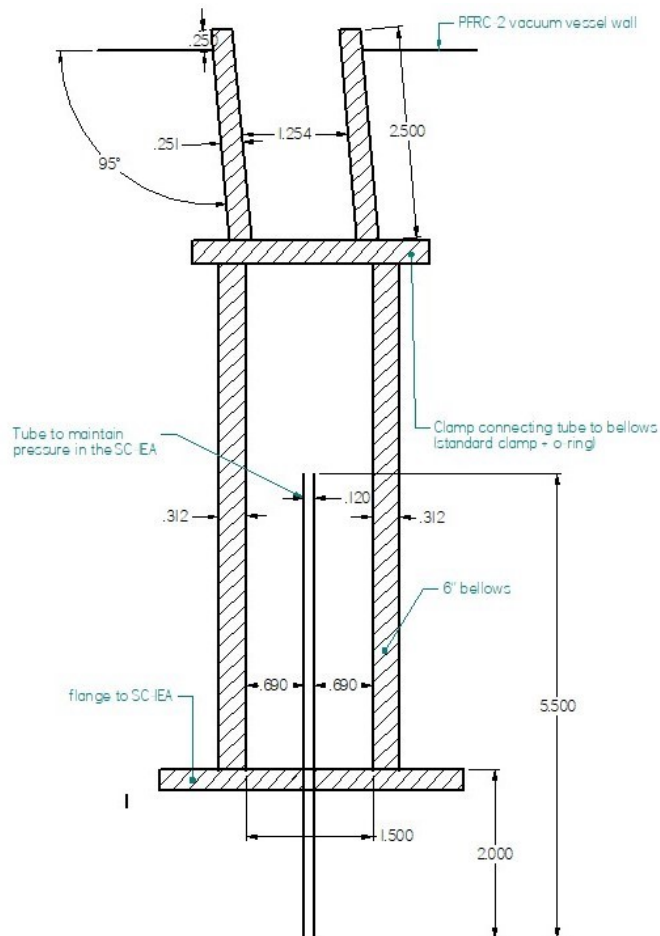


Figure 30: Plans for the tubing between the PFRC-2 and the SC-IEA vessels. The tube's dimensions in the present plans have the diameter of the conductive tube at 0.3" and the length at 4".

Figure 30 displays a bird's eye view of the plans drawn out for the installation of the port tubing. The top of the figure is the PFRC-2 vessel wall, and the bottom of the

figure is the SC-IEA diagnostic vessel. The three main components of the connection are pictured in the figure: the polycarbonate tube entering the vacuum vessel, the stainless steel bellows, and the low conductance thin tube connecting between the bellows and the SC-IEA vessel.

## 4.2 Maintaining Vacuum

In order to maintain low pressure ( $\lesssim 10^{-6}$  Torr) in the SC-IEA port crosses while they are connected to the PFRC-2, which is kept at a pressure of  $\lesssim 10^{-3}$  Torr, there will be a long, thin tube placed in the center of the bellows which connects the SC-IEA and the PFRC-2. This conducting tube is designed to have a conductance low enough to keep the pressure at the desirable level in the SC-IEA. A low pressure is required to minimize losses due to scattering out of the detector path as well as to maximize the lifetime of the getter pumps.

The first step in determining the proper dimensions with which to construct the low-conductance tube is to determine the conductance of a tube as a function of length and radius. In Chapter 2 of *Scientific Foundations of Vacuum Technique*, [20], Dushman states that flow through a pipe or orifice can be described using three different models: laminar, molecular, or a transition region between the two. In laminar flow, the flow is dominated by collisions between the gas particles rather than with the pipe, whereas in molecular flow, the flow is dominated by interactions with the pipe. Therefore, molecular flow is largely determined by the geometric characteristics of the apparatus while laminar flow is mostly independent of these characteristics. The applicability of these two flow models is determined by relative frequencies of collisions between molecules and collisions between molecules and the walls. To compare these frequencies, one uses the mean free path,  $\bar{l}$ , and a characteristic measurement of the pipe, such as its radius,  $a$ . If the mean free path is much larger than the radius, then the flow is molecular, if the mean free path is much smaller than the radius, the flow is laminar. If there is no great difference between the frequencies of these two collisions, then the flow is in the regime in which both collisions between molecules and collisions between molecules and walls need to be

taken into account. Dushman gives simple criteria for this relative frequency:

$$\begin{aligned}\bar{l}/a < 0.01 &\longrightarrow \text{laminar} \\ \bar{l}/a > 1.00 &\longrightarrow \text{molecular} \\ 0.01 < \bar{l}/a < 1.00 &\longrightarrow \text{transition,}\end{aligned}$$

where  $\bar{l}$  is the mean free path and  $a$  is the characteristic dimension.

In this case, the characteristic dimension used is the radius of the pipe, which will be 0.15" = 0.381 cm. The mean free path for H<sub>2</sub> gas at 300 K can be found using:

$$\bar{l} = \frac{1}{4\pi r^2} \frac{1}{n} = \frac{k_B T}{\pi d^2 P}, \quad (38)$$

which is found in [2]. In SI units, 0.001 Torr = 0.13 Pa, and  $k_B = 1.38 * 10^{-23}$  J/K. Plugging in these values, and assuming that the molecular diameter of H<sub>2</sub> is < 1 Angstrom or  $10^{-10}$  m, which is the value given for oxygen in [2], the mean free path of H<sub>2</sub> is  $\approx 100$  cm. Using this mean free path and the characteristic dimension of radius for the tube to be used,  $a = 0.381$  cm, the ratio  $\bar{l}/a \approx 266$ , which safely puts this flow in the range of molecular flow.

For the conductance of a tube using molecular flow, Dushman (2.29a) writes that:

$$C = 30.48 \left( \frac{a^3}{l} \right) \sqrt{\frac{T}{M}} \text{ L/s}, \quad (39)$$

where  $a$  (radius) and  $l$  (tube length) are measured in centimeters,  $T$  is measured in Kelvin, and  $M$  is the molar mass of the gas. Figure 31 shows the conductance calculated from Equation 39 as a function of tube radius for tubes of varying length. The dashed black line marks the diameter and conductance calculated for the tube to be used in practice, a tube with inner diameter of 0.3" and a length of 4.0". With these dimensions, the conductance is calculated to be  $\approx 2.0$  L/s.

To calculate the steady-state pressure in the SC-IEA, one posits that the system is at steady state when the molecular current ( $\frac{dn_1}{dt}$ ) into the port cross is the same as the molecular current ( $\frac{dn_2}{dt}$ ) out of the port cross. One can use the throughput (pumping speed ( $C$ ) \* pressure ( $P$ )) as the molecular current. To illustrate this, differentiating both sides shows that, if  $\frac{dP}{dt} = 0$ , i.e. at steady state, then  $P \frac{dV}{dt} = Q = \frac{dN}{dt} kT$ . Thus, the throughput,  $Q$ , is proportional to the molecular current into/out of the vessel. As

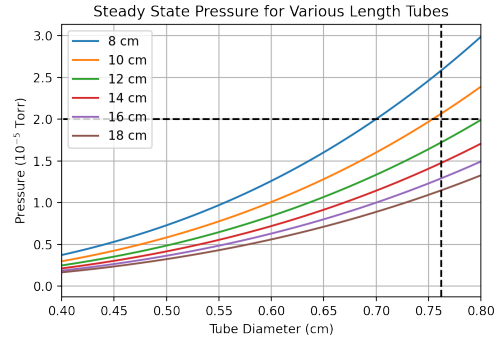
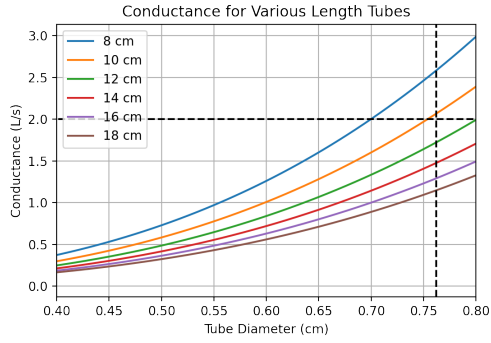


Figure 31: Conductance of a tube of length  $l$  as a function of tube diameter. Figure 32: Pressure in SC-IEA chamber assuming a pumping speed of 350 L/s.

described in its manual, the turbo pump (Turbo V-551) used on the machine had a lowest possible pumping speed of 350 L/s. Because the Turbo pumps from the end of a tube, with several connections, a lower pumping speed of  $\approx 100$  L/s will be assumed. At steady state, then, the throughput into the port cross from the tube must equal the throughput out of the port cross due to the turbo pump, i.e.:

$$\begin{aligned}
 Q_1 P_1 &= Q_2 P_2 \\
 2.0 \text{ L/s} * 10^{-3} \text{ Torr} &= 100 \text{ L/s} * P_2 \\
 P_2 &= 2.0 * 10^{-5} \text{ Torr}.
 \end{aligned}$$

This same calculation is performed assuming the turbo's pumping speed of 100 L/s for various different lengths of tube in Figure 32. One can see the general scaling of the conductance and pressure. From those calculations, it is evident that a wide range of lengths and diameters would be suitable for maintaining workable pressure in the SC-IEA. Nevertheless, to be safe, a tube length of 10.16 cm (4.00"), about the length of the stainless steel bellows will be used, while keeping a slightly larger diameter of 0.762 cm (0.3") to make alignment with the stripping cell simpler. Even if the pumping speed is only 100 L/s, the pressure in the SC-IEA should only be  $\approx 2.00 * 10^{-5}$  Torr, which is still a safe range for the maintenance of the getter pumps.

To summarize, the desired parameters of the connection have been presented, along with a practical plan for the connection, along with an analysis of the pressure in the port crosses due to the connection to the PFRC-2.

## 5 Conclusion

To conclude, this thesis has attempted to describe the physics that contribute to the operation of the charge exchange ion-energy analyzer, with a particular focus on the specific ion dynamics in the analyzer, along with an experimental test of the properties of the analyzer due to those ion dynamics. The quantities established through the process of calibration will prove useful in the operation of the diagnostic on the PFRC-2, when the physics of the diagnostic will be tested further and have significant implications for the interpretation of the energy distribution of neutrals tested with the system. This thesis has worked on building the framework for interpreting the signal that comes from the diagnostic, through calibration with a known source as well as through testing the effects that uncertainties in quantities like the resolution, the energy-voltage relation, and the energy dependence of the ionization efficiency of the stripping cell.

Headway has been made in the construction and calibration of the diagnostic, but the main part of the work remains to be performed and tested. Future work includes the operation of the PFRC-2 with the charge exchange diagnostic and the interpretation of the data from the SC-IEA. The work performed as part of this thesis has hopefully aided the group in the advancement of this exciting project to develop a system to sensitively measure the ion energy distribution.

## Appendix I: Derivation of Binet's Equation<sup>9</sup>

In deriving the approximate path of ions through the curved-plate analyzer, use is made of Binet's Equation, a differential equation governing the path  $u(\theta)$ , where  $u = \frac{1}{r}$  of a particle in a central force field. First, the Lagrangian of a particle in a central potential  $U(r)$  is written down, along with the Euler-Lagrange Equations for the two degrees of freedom:

$$L = \frac{1}{2}m \left( \dot{r}^2 + r^2\dot{\theta}^2 \right) - U(r) \quad (40)$$

$$\frac{\partial L}{\partial \dot{\theta}} = mr^2\dot{\theta} = \text{constant} = l \quad (41)$$

$$m\ddot{r} = mr\dot{\theta}^2 - \partial_r U = mr\dot{\theta}^2 + F(r). \quad (42)$$

Now, we let  $u = \frac{1}{r}$  and take the first derivative with respect to  $\theta$ :

$$\frac{du}{d\theta} = \frac{dr}{d\theta} \frac{du}{dr} = -\frac{1}{r^2} \frac{dr}{dt} \frac{dt}{d\theta} = -\frac{1}{r^2} \frac{\dot{r}}{\dot{\theta}}. \quad (43)$$

Using conservation of angular momentum (i.e. the  $\theta$  Euler-Lagrange Equation), one can write:  $\frac{du}{d\theta} = -\frac{m}{l}\dot{r}$ . Differentiating once more, it is found that:

$$\frac{d^2u}{d\theta^2} = -\frac{m}{l} \frac{d\dot{r}}{d\theta} = -\frac{m}{l} \frac{d\dot{r}}{dt} \frac{dt}{d\theta} = -\frac{m}{l} \frac{\ddot{r}}{\dot{\theta}}. \quad (44)$$

Using the Euler-Lagrange Equation for  $r$  and substituting in for  $\dot{\theta} = \frac{l}{mr^2}$ , it is found that:

$$\frac{d^2u}{d\theta^2} = -\frac{mr^2}{l^2} \left( mr\dot{\theta}^2 + F(r) \right).$$

Substituting in  $l^2 = m^2r^4\dot{\theta}^2$  and  $u = \frac{1}{r}$ , the final form of Binet's Equation is found to be:

$$\frac{d^2u}{d\theta^2} + u = -\frac{m}{l^2u^2}F(u). \quad (45)$$

Using this form, one can easily plug in for different forms of  $F(u)$  to arrive at equations for the trajectories of the orbits  $u(\theta)$ . For the case of the curved-plate analyzer, for which  $F \propto u$ , Binet's Equation yields a clear starting point for solving the trajectory.

---

<sup>9</sup>This derivation largely follows that in Thornton and Marion Section 8.4.

## References

- [1] F. F. Chen, *Introduction to Plasma Physics* (Springer, 1974).
- [2] D. Schroeder, *An Introduction to Thermal Physics* (Addison Wesley, 1999).
- [3] S. A. Cohen, A. S. Landsman, and A. H. Glasser, *Stochastic ion heating in a field-reversed configuration geometry by rotating magnetic fields*, *Physics of Plasmas* **14**, 072508 (2007), <https://doi.org/10.1063/1.2746813>.
- [4] H.-S. Bosch and G. Hale, *Improved formulas for fusion cross-sections and thermal reactivities*, *Nuclear Fusion* **32**, 611 (1992).
- [5] I. H. Hutchinson, *Neutral atom diagnostics*, 2 ed. (Cambridge University Press, 2002), p. 322–368.
- [6] D. Rapp and I. B. Ortenburger, *Interchange of Charge between Gaseous Molecules*, *The Journal of Chemical Physics* **33**, 1230 (1960), <https://doi.org/10.1063/1.1731361>.
- [7] R. J. Colchin, A. L. Roquemore, and S. D. Scott, *Charge exchange stripping cell measurements over a wide pressure range*, *Review of Scientific Instruments* **59**, 1667 (1988), <https://doi.org/10.1063/1.1140127>.
- [8] P. Beiersdorfer, A. L. Roquemore, and R. Kaita, *Characteristics of compact solid-target charge exchange analyzers for energetic ion diagnostics on tokamaks*, *Review of Scientific Instruments* **58**, 2092 (1987), <https://doi.org/10.1063/1.1139469>.
- [9] H. P. Eubank and T. D. Wilkerson, *Ion Energy Analyzer for Plasma Measurements*, *Review of Scientific Instruments* **34**, 12 (1963), <https://doi.org/10.1063/1.1718108>.
- [10] S. S. Medley and A. L. Roquemore, *Construction and operation of parallel electric and magnetic field spectrometers for mass/energy resolved multi-ion charge exchange diagnostics on the Tokamak Fusion Test Reactor*, *Review of Scientific Instruments* **69**, 2651 (1998), <https://doi.org/10.1063/1.1148994>.
- [11] K. Hayashi *et al.*, *Charge exchange neutral particle mass and energy analyzer for the JT-60 tokamak*, *Review of Scientific Instruments* **56**, 359 (1985), <https://doi.org/10.1063/1.1138303>.

- [12] L. C. Steinhauer, *Review of field-reversed configurations*, Physics of Plasmas **18**, 070501 (2011), <https://doi.org/10.1063/1.3613680>.
- [13] S. A. Cohen and R. D. Milroy, *Maintaining the closed magnetic-field-line topology of a field-reversed configuration with the addition of static transverse magnetic fields*, Physics of Plasmas **7**, 2539 (2000), <https://doi.org/10.1063/1.874094>.
- [14] S. A. Cohen and A. H. Glasser, *Ion Heating in the Field-Reversed Configuration by Rotating Magnetic Fields near the Ion-Cyclotron Resonance*, Phys. Rev. Lett. **85**, 5114 (2000).
- [15] A. S. Landsman, S. A. Cohen, and A. H. Glasser, *Regular and stochastic orbits of ions in a highly prolate field-reversed configuration*, Physics of Plasmas **11**, 947 (2004), <https://doi.org/10.1063/1.1638751>.
- [16] S. A. Cohen *et al.*, *Formation of Collisionless High- $\beta$  Plasmas by Odd-Parity Rotating Magnetic Fields*, Phys. Rev. Lett. **98**, 145002 (2007).
- [17] A. L. Hughes and V. Rojansky, *On the Analysis of Electronic Velocities by Electrostatic Means*, Phys. Rev. **34**, 284 (1929).
- [18] J. H. Adlam and D. A. Aldcroft, *The Measurement of the Efficiency of a Helium Gas Cell for the Conversion of a Beam of Energetic Atomic Hydrogen into a Proton Beam*, CLM-R100 (1969).
- [19] C. F. Barnett *et al.*, *Atomic data for controlled fusion research*, (1977).
- [20] S. Dushman, *Scientific Foundations of Vacuum Technique* (J. Wiley, 1949).

## Acknowledgements

Thank you to Professor Samuel A. Cohen for his guidance in this project. Thank you to Bruce Berlinger for his technical expertise and aid. Thank you to Dr. Shota Abe for his guidance in the operation of the ion gun. Thank you to Dr. Alan Glasser and Dr. Alex Glasser for their help with simulations. The diagnostic was designed and purchased by Eugene Evans. Thank you to Atara Kelman for her ongoing support.

The template for this thesis is modified from the Junior Paper template found on the Physics Department website and was made by Nicole Ozdowski.